QUANTUM GASES IN ROTATING OPTICAL LATTICES

A DISSERTATION SUBMITTED TO
THE DEPARTMENT OF PHYSICS
AND THE INSTITUTE OF ENGINEERING AND SCIENCE
OF BILKENT UNIVERSITY
IN PARTIAL FULFILLMENT OF THE REQUIREMENTS
FOR THE DEGREE OF
DOCTOR OF PHILOSOPHY

By
Rifat Onur Umucalılar
August, 2010

I certify that I have read this thesis and that in my opinion it is fully adequate, in scope and in quality, as a dissertation for the degree of Doctor of Philosophy.

Assoc. Prof. Dr. Mehmet Özgür Oktel (Advisor)

I certify that I have read this thesis and that in my opinion it is fully adequate, in scope and in quality, as a dissertation for the degree of Doctor of Philosophy.

Prof. Dr. Bilal Tanatar

I certify that I have read this thesis and that in my opinion it is fully adequate, in scope and in quality, as a dissertation for the degree of Doctor of Philosophy.

Assoc. Prof. Dr. Oğuz Gülseren

I certify that I have read this thesis and that in my opinion it is fully adequate, in scope and in quality, as a dissertation for the degree of Doctor of Philosophy.

Assoc. Prof. Dr. Ergün Yalçın

I certify that I have read this thesis and that in my opinion it is fully adequate, in scope and in quality, as a dissertation for the degree of Doctor of Philosophy.

Assoc. Prof. Dr. Bayram Tekin

Approved for the Institute of Engineering and Science:

Prof. Dr. Levent Onural
Director of Institute of Engineering and Science

ABSTRACT

Quantum Gases in Rotating Optical Lattices

Rifat Onur Umucalılar
Ph.D. in Physics
Supervisor: Assoc. Prof. Mehmet Özgür Oktel
August, 2010

The thesis is structured into two main parts so as to cover bosons and fermions in rotating optical lattices separately. In the first part, after a brief introduction to ultracold atoms in optical lattices, we review the single-particle physics for the lowest (s) band of a periodic potential under an artificial magnetic field created by rotation. Next, we discuss rotational effects on the first excited (p) band of the lattice, extending the methods available for the lowest band. We conclude the first part with a discussion of many-body physics in rotating lattice systems using a mean-field approach and investigate how the transition boundary between superfluid and Mott insulator phases is affected by the single-particle spectrum. In this context, we also examine a possible coexistent phase of Mott insulator and bosonic fractional quantum Hall states, appearing for certain system parameters near the Mott insulator lobes in the phase diagram.

The second part starts with the proposal of a realization and detection scheme for the so-called topological Hofstadter insulator, which basically reveals the single-particle spectrum discussed before. The scheme depends on a measurement of the density profile for noninteracting fermions in a rotating optical lattice with a superimposed harmonic trapping potential. This method also allows one to measure the quantized Hall conductance, a feature which appears when the Fermi energy lies in an energy gap of the lattice potential. Finally, we explore the Bardeen-Cooper-Schrieffer type of pairing of fermionic atoms in optical lattices under an artificial magnetic field by paying special attention to single-particle degeneracies and present our results for the vortex lattice structure of the paired fermionic superfluid phase.

Keywords: Ultracold atoms, rotating optical lattices, artificial magnetic field, superfluid-Mott insulator transition, bosonic fractional quantum Hall states, p band, topological Hofstadter insulator, Bardeen-Cooper-Schrieffer type of pairing, vortex lattice.

ÖZET

Dönen Optik Örgülerde Kuvantum Gazları

Rifat Onur Umucalılar
Fizik, Doktora
Tez Yöneticisi: Doç. Dr. Mehmet Özgür Oktel
Ağustos, 2010

Bu tez, dönen optik örgü sistemlerinde bozonlar ve fermiyonlar ayrı ayrı incelenecek şekilde iki ana bölüm halinde düzenlenmiştir. İlk bölümde, optik örgülerdeki ultrasoğuk atomlara kısa bir girişten sonra, dönmenin yarattığı yapay manyetik alan altında ve periyodik bir potansiyeldeki tek parçacık fiziği en düşük enerjili bant (s bandı) için gözden geçirilmektedir. Ardından, s bandı için kullanılan yöntemler genişletilerek, dönmenin ilk uyarılmış bant (p bandı) üzerindeki etkilerine değinilmiştir. İlk bölümde son olarak, dönen örgü sistemlerindeki çok parçacık fiziği ortalama alan yöntemi kullanılarak ele alınmakta ve süperakışkan–Mott yalıtkanı faz geçiş sınırına tek parçacık spektrumunun etkileri araştırılmaktadır. Bu bağlamda, bazı sistem parametreleri için faz diyagramında Mott yalıtkanı yakınlarında ortaya çıkması olası, Mott yalıtkanı ve bozonik kesirli kuvantum Hall durumlarının birlikte var olduğu bir faz da incelenmiştir.

İkinci bölüm, temelde, daha önce ele alınmış olan tek parçacık spektrumunu açığa çıkaran, topolojik Hofstadter yalıtkanının gözlenmesi için bir yöntem önerisiyle başlamaktadır. Bu yöntem, dönen bir optik örgüye ek olarak uygulanan harmonik tuzaklama potansiyeli içindeki birbiriyle etkileşmeyen fermiyonların yoğunluk dağılımının ölçülmesine dayanmaktadır. Yöntem aynı zamanda, Fermi enerjisi örgü potansiyelinin yasak bir enerji aralığında bulunduğunda ortaya çıkan bir özellik olan kesikli Hall iletkenliğinin ölçülmesine de olanak sağlamaktadır. Son olarak, yapay manyetik alan altındaki bir optik örgüde bulunan fermiyonik atomların Bardeen-Cooper-Schrieffer türü eşleşmeleri, tek parçacık yozluklarına özel önem verilerek incelenmiş ve eşlenmiş fermiyonik süperakışkan fazının girdap örgüsü yapısı için elde edilen sonuçlar sunulmuştur.

Anahtar Sözcükler: Ultrasoğuk atomlar, dönen optik örgüler, yapay manyetik alan, süperakışkan-Mott yalıtkanı faz geçişi, bozonik kesirli kuvantum Hall durumları, p bandı, topolojik Hofstadter yalıtkanı, Bardeen-Cooper-Schrieffer türü eşleşme, girdap örgüsü.

Anneme ve babamın değerli anısına

Acknowledgement

In the course of my Ph.D. study, I had invaluable collaborations and friendships. The first person I would like to thank is, not surprisingly, my thesis supervisor Assoc. Prof. Dr. Mehmet Özgür Oktel, to whom I am greatly indebted for his intense efforts in guiding me in all kinds of subjects, academic or not. I am also very grateful to Assoc. Prof. Dr. Erich Mueller (Cornell University) and Dr. Hui Zhai (Institute for Advanced Study, Tsinghua University) from whom I learned a lot.

My dear friends Barış Öztop, Levent Subaşı, Murat Keçeli, Nadir Ghazanfari and Sevilay Sevinçli deserve special thanks for their helps and joyful companionship through years.

Finally, I just cannot thank my family members enough for their motivating support and trust in me.

Contents

List of Figures

List of Tables

Chapter 1

Introduction

As it is common in most introductory texts and reviews or even research articles dealing with ultracold atoms in optical lattices, this introduction starts with a brief praise for the merits of these many-body systems. The study of cold atoms made a huge step when Bose-Einstein condensation in dilute gases was first observed in 1995 thanks to advanced cooling techniques [1, 2]. The demonstration of coherent matter waves related to the macroscopic occupation of a single quantum state was not only a solid support for a theoretical conjecture established long before [3] but also made connections to some condensed matter phenomena like superfluidity, which in turn led to other predictions and new experimental possibilities that are not achievable in conventional condensed matter systems. This is a generic feature of cold-atom physics and has been even more pronounced with the use of cold atoms in optical lattices in 2002 as a tool for studying strongly correlated quantum phenomena [4], which evidenced a quantum phase transition between superfluid and insulator phases of atoms in the lattice as predicted theoretically [5, 6]. The flexible parameters of optical lattices make them perfect candidates to test certain condensed matter theories that have not been yet verified rigorously. But still, these systems are inherently different from condensed matter systems and one has to use different techniques to be able to simulate the condensed matter analogues. For instance, as almost all optical lattice experiments are done with neutral atoms, in order to simulate the effects of magnetic field on a charged particle, rotation or some other kind of arrangement, like direct phase imprinting using atom-light interactions, should be introduced. As this synthetic magnetic field couples only to the orbital degree of freedom and not to the spin of the particles, one can observe new phenomena in which no Zeeman shift is involved. Artificial gauge fields in optical lattices also allow one to study the physics of vortex lattices and investigate strongly correlated systems, like the analogues of fractional quantum Hall states. This simulative power and the relative ease of control of ultracold atoms in optical lattices along with other well-established techniques of atomic physics, such as the use of Feshbach resonances to tune the interactions between atoms, provide researchers with both a better understanding of the previously predicted phenomena and a valuable medium for new applications, among which those related to quantum information processing are perhaps the most popular nowadays [7].

1.1 Optical Lattices

Optical lattices are periodic structures of varying light intensity formed by the interference of counter-propagating laser beams. The trapping of atoms in these structures is possible due to the interaction of the laser field with the induced dipole moment of atoms which is again created by the field itself (or one may equivalently say that the atom experiences an external potential as its energy is shifted by the space dependent electric field). The dipole force acting on an atom in an off-resonant laser field with frequency ω_L and time-averaged electric field intensity $|\mathbf{E}(\mathbf{r})|^2$ is

$$\mathbf{F} = \frac{1}{2}\alpha(\omega_L)\nabla[|\mathbf{E}(\mathbf{r})|^2], \tag{1.1}$$

where $\alpha(\omega_L) \approx |\langle e|\hat{d}|g\rangle|^2/\hbar(\omega_0 - \omega_L)$ is the real part of the dynamical polarizability of the atom, $\hbar\omega_0$ being the energy difference between the ground state $|g\rangle$ and the excited state $|e\rangle$, and $\hat{d}$ is the dipole operator in the direction of the field [8, 9]. For red ($\omega_L < \omega_0$) or blue ($\omega_L > \omega_0$) detuned laser beams, atoms are attracted to or repelled from an intensity maximum in space, respectively.

The rate of loss of atoms from the ground state is determined by the imaginary part of polarizability.

When two counter-propagating beams with wavelength λ interfere, a standing wave pattern in one dimension with period $a = \lambda/2$ occurs (it is possible to obtain larger periods by directing beams towards each other at angles smaller than 180°). By overlapping two or three standing waves, two and three dimensional optical potentials can be created. The resulting potential at the center of the trap can be approximated to be $V(\mathbf{r}) = V_0 \sum_{i=1}^{d} \sin^2(kr_i)$, where $d = 1, 2, 3$ denotes dimension, $k = 2\pi/\lambda$, and V_0 is the strength of the potential. For sufficiently deep potentials, the potential around a single site is almost harmonic with frequency ω_0 and the following relation holds: $\hbar\omega_0 \approx 2E_R(V_0/E_R)^{1/2}$, where $E_R = \hbar^2k^2/2m$ (m being the atomic mass) is called the recoil energy, which is a natural energy scale for optical lattices. Again in this deep lattice limit ($V_0, \hbar\omega_0 \gg E_R$) and for low temperatures, atoms settle to the lowest vibrational level of each site and the energy as a function of quasi-momentum $\mathbf{q}$, $\varepsilon(\mathbf{q}) = -2t\sum_{i=1}^{d} \cos(q_i a) + d\hbar\omega_0/2$ is of typical tight-binding form. Here $t > 0$ is the tunneling amplitude (or gain in kinetic energy due to tunneling) between nearest-neighbor sites given by the following matrix element of the single-particle Hamiltonian

$$t = \int w_0^*(\mathbf{r})[\frac{-\hbar^2\nabla^2}{2m} + V(\mathbf{r})]w_0(\mathbf{r} + a\mathbf{e}_\nu)d\mathbf{r}, \tag{1.2}$$

where $\mathbf{e}_\nu$ is the unit vector along the ν direction and $w_n(\mathbf{r} - \mathbf{R})$ is the localized Wannier function at site $\mathbf{R}$ corresponding to the nth Bloch band (we take $n = 0$ in the above integral to denote the lowest band) [6]. Wannier functions form an orthonormal and complete basis and are related to the exact eigenfunctions of the periodic potential, namely Bloch wave functions $\psi_{n,\mathbf{q}}(\mathbf{r})$, via a Fourier transform: $\psi_{n,\mathbf{q}}(\mathbf{r}) = \sum_{\mathbf{R}} w_n(\mathbf{r} - \mathbf{R}) \exp(i\mathbf{q} \cdot \mathbf{R})$.

1.2 Bose-Hubbard Hamiltonian and Superfluid-Mott Insulator Transition

To describe many-particle physics in optical lattices, one may resort to the language of second quantization. The field operator $\hat{\psi}(\mathbf{r})$ annihilating a particle at point $\mathbf{r}$ can be expanded in terms of the Wannier functions, as they form a complete basis

$$\hat{\psi}(\mathbf{r}) = \sum_{\mathbf{R}} w_n(\mathbf{r} - \mathbf{R}) a_{\mathbf{R},n}, \tag{1.3}$$

where $a_{\mathbf{R},n}$ is the destruction operator for the Wannier state. Within a pseudo-potential approach valid for sufficiently low temperatures, two-body interactions between atoms are described by the following Hamiltonian

$$H_{int} = \frac{g}{2} \int d\mathbf{r} \hat{\psi}^{\dagger}(\mathbf{r}) \hat{\psi}^{\dagger}(\mathbf{r}) \hat{\psi}(\mathbf{r}) \hat{\psi}(\mathbf{r}), \tag{1.4}$$

where $g = 4\pi\hbar^2 a_s/m$ is the interaction strength determined by the s-wave scattering length a_s. This form includes interactions between particles in all Wannier states, as can be seen by inserting Eq. (1.3) into Eq. (1.4). However, if we consider the deep lattice limit and assume only the lowest band is populated, the on-site term $Un_{\mathbf{R}}(n_{\mathbf{R}} - 1)/2$ characterizes the dominant interaction for bosons (for fermions with two possible spin states $|\uparrow\rangle$ and $|\downarrow\rangle$, the analogous term would be $Un_{\mathbf{R},\uparrow} n_{\mathbf{R},\downarrow}$). Here, $n_{\mathbf{R}} = a^{\dagger}_{\mathbf{R},0} a_{\mathbf{R},0}$ is the number operator for the lowest band Wannier state and U is given by

$$U = g \int d\mathbf{r} |w_0(\mathbf{r})|^4 \approx \sqrt{8/\pi} k a_s E_R (V_0/E_R)^{(3/4)}. \tag{1.5}$$

The last approximate equality is derived by taking the Wannier state as the ground state of the local harmonic potential [8].

A model Hamiltonian describing bosonic particles in optical lattices can then be constructed under the assumptions that the Wannier functions are well-localized so that only nearest-neighbor tunneling should be taken into account and the energy gap between the lowest band and the first excited band is much larger than both the energy of local oscillations and the effective interaction energy between particles. Using t from Eq. (1.2) and U from Eq.

(1.5), we can write the so-called Bose-Hubbard Hamiltonian as

$$H_{BH} = -t \sum_{\langle i,j \rangle} a_i^\dagger a_j + \frac{U}{2} \sum_i n_i(n_i - 1) + \sum_i (\epsilon_i - \mu) n_i, \tag{1.6}$$

where i and j are site indices, $\langle i, j \rangle$ denotes summation over nearest-neighbor sites, ϵ_i is the energy shift for the ith site due to disorder or an external trapping potential, and μ is the chemical potential that fixes the particle number [6]. The first term in Eq. (1.6) is referred to as the hopping term and gives the kinetic energy gain due to tunneling of particles to nearest-neighbor sites. It is the competition between this term and the on-site repulsive interaction term, which energetically disfavors the existence of more than one particle at a given site, that determines the phase of the system. By tuning the parameter t/U, it is possible to drive a quantum phase transition at zero temperature ($T = 0$) between an insulator phase and a superfluid phase.

At $T = 0$ and in the limit $U \to 0$, the system is expected to be a perfect superfluid (SF) of the form

$$|\Psi_{SF}\rangle = \frac{1}{\sqrt{N!}} \left(\frac{1}{\sqrt{N_s}} \sum_i a_i^\dagger \right)^N |0\rangle, \tag{1.7}$$

where N is the number of particles, N_s is the number of lattice sites, and $|0\rangle$ denotes the vacuum state. In this phase, all the particles occupy the $\mathbf{q} = 0$ state of the lowest band. In the opposite limit $t \to 0$, where tunneling is totally suppressed, minimization of the on-site interaction energy leads to the so-called Mott insulator (MI) phase with equal number of particles n_0 (for commensurate systems with $N/N_s = n_0$) at each site (for brevity, we will frequently call this phase 'Mott state' or 'Mott phase'). This state can be written as a product of local Fock (or number) states:

$$|\Psi_{MI}\rangle = \frac{1}{\sqrt{n_0!}} \prod_i (a_i^\dagger)^{n_0} |0\rangle. \tag{1.8}$$

In an infinite lattice with finite particle density, the superfluid state [Eq. (1.7)] very much resembles a coherent state that can be written as a product of local coherent states as the Bose operators for different sites commute. As a consequence of the fact that in both limits (t or $U \to 0$) the state can be cast into a product form, one can make the following variational Gutzwiller ansatz [10] for arbitrary t/U

$$|\Psi_{GW}\rangle = \prod_i \left(\sum_{n=0}^{\infty} c_n |n\rangle_i \right), \tag{1.9}$$

which approximates the state as a product of local states written in the number basis. Next step is to minimize the energy with respect to the expansion coefficients c_n for a given t/U to find the ground state of the system. An equivalent way to do that is to perform a self-consistent mean-field calculation [11, 12], in which one constructs the superfluid order parameter $\psi = \langle \Psi_{GW}|a_i|\Psi_{GW}\rangle$, which is zero for the Mott state and nonzero for the superfluid state, and reduce the Bose-Hubbard Hamiltonian [Eq. (1.6)] into a sum over single-site terms. This reduction is achieved by assuming the expected value of a_i for the true ground state fluctuates around the mean-field ψ and regarding $(a_i - \psi)$ as a small quantity. Upon expansion of the Hamiltonian to first order in this small quantity [which can be done by inserting the equality $a_i = \psi + (a_i - \psi)$ into the Hamiltonian and keeping terms only first order in $(a_i - \psi)$], one gets single-site terms. Using a truncated number basis with sufficient number of particles per site (determined by the convergence of results) and starting with an initial set of c_n, one then diagonalizes the single-site Hamiltonian, feeding back the new c_n for the lowest energy state at each step until self-consistency is reached.

If one is interested only in finding an analytical form for the transition boundary between the Mott and superfluid phases in the μ–t phase diagram, there is an easier method to pursue, again within mean-field theory. Close to the transition, the number of particles at an arbitrary site cannot be much different from the integer occupation n_0 and fluctuates around it. One can then assume only one particle or hole excitation takes place at each site and make the following ansatz for the ground state

$$|G\rangle = \Delta|n_0 - 1\rangle + |n_0\rangle + \Delta'|n_0 + 1\rangle, \tag{1.10}$$

which is the same for every site in a homogenous system. Minimization of the resulting energy with respect to Δ and Δ' leads to a formula for the transition

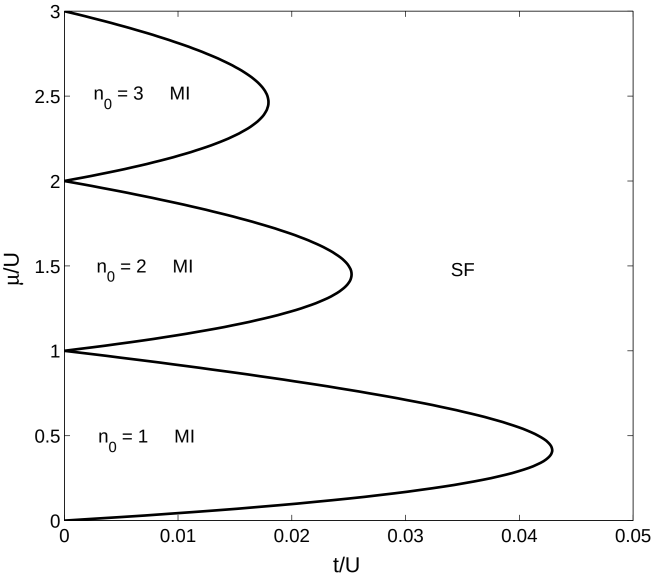

Figure 1.1: Superfluid (SF)–Mott insulator (MI) phase diagram for a square lattice at zero temperature. The transition boundary is calculated in the mean-field approximation. n_0 is the number of particles at each site in the Mott insulator phase.

boundary (for a square lattice) given by

$$(t/U)_{\text{critical}} = \frac{(n_0 - \mu/U)[1 - (n_0 - \mu/U)]}{4(1 + \mu/U)}, \tag{1.11}$$

where $n_0 - 1 \leq \mu/U \leq n_0$. The details of a similar calculation for the inhomogeneous case where an effective external magnetic field is present will be given in the next chapter. The zero temperature phase diagram determined by Eq. (1.11) is shown in Fig. 1.1.

While the number of particles at each site is fixed in the Mott insulator state, the number distribution is Poissonian in the superfluid phase. In contrast to a well-defined particle number per site, there is no phase coherence in the Mott phase, whereas the superfluid has phase coherence. In time-of-flight experiments, where the atoms are allowed to expand freely after trapping and lattice potentials are turned off, this marked difference can be observed clearly [4]. If the system is in the superfluid phase prior to free expansion, there appear sharp interference peaks in the absorption image reflecting the initial momentum distribution (multiple peaks appear due to the lattice potential). For the Mott phase, the interference image is blurred. Another difference between these two phases lies in their excitation spectrum. Mott phase has a finite excitation gap (to add one more particle one has to provide energy of magnitude U) and therefore the system is incompressible. There is no gap in the excitation spectrum of a superfluid and the system has finite compressibility in this case. In the presence of an external trapping potential, the density profile has the so-called wedding-cake shape, which can be accounted for by different compressibilities of the two phases. The incompressible Mott phases for different n_0 are observed as plateaus which are separated by compressible superfluid layers. This structure can most easily be understood by assuming that the trapping potential varies smoothly in space so that the local density approximation (LDA) is valid. In this approximation, one constructs a space dependent chemical potential $\mu(\mathbf{r}) = \mu - V_{\text{trap}}(\mathbf{r})$ which controls the spatial distribution of particle density. By following a straight trajectory for a given t/U in Fig. 1.1, one can then see that the system repeatedly enters the superfluid and Mott phases [6, 8].

1.3 Rotating Optical Lattices

As mentioned before, magnetic field–charged particle interaction can be simulated in a variety of ways in cold-atom systems. One conceptually simple method to create an artificial magnetic field is to rotate the system [8, 13, 14]. This can be seen by investigating the Hamiltonian for a particle in the rotating frame of a two-dimensional system

$$H_{rot} = \frac{1}{2m}\mathbf{p}_\perp^2 + \frac{1}{2}m\omega_\perp^2(x^2+y^2) - \Omega\hat{\mathbf{z}}\cdot\mathbf{r}\times\mathbf{p}_\perp, \tag{1.12}$$

where $\mathbf{p}_\perp = (p_x, p_y)$, $\mathbf{r} = (x, y)$, $\omega_\perp$ is the transverse harmonic trapping frequency, and Ω is the rotation frequency. This Hamiltonian can be rearranged as follows

$$H_{rot} = \frac{(\mathbf{p}_\perp - m\Omega\hat{\mathbf{z}}\times\mathbf{r})^2}{2m} + \frac{1}{2}m(\omega_\perp^2 - \Omega^2)(x^2+y^2). \tag{1.13}$$

If Ω is equal to $\omega_\perp$, the last term vanishes and the Hamiltonian is formally identical to that of a particle of charge e (which can be positive or negative) in a magnetic vector potential $\mathbf{A} = (m\Omega/e)\hat{\mathbf{z}}\times\mathbf{r}$ (called the symmetric gauge vector potential), which correspondingly gives the effective magnetic field as $\mathbf{B} = \nabla \times \mathbf{A} = (2m\Omega/e)\hat{\mathbf{z}}$. The eigenstates of this Hamiltonian are the celebrated Landau levels, which are infinitely degenerate. If one retains the last term, the problem is still exactly solvable, but the degeneracy of the Landau levels are now broken. Nevertheless, one can speak about definite Landau levels (or branches) if Ω is very close to $\omega_\perp$ and the separation between two such branches is much larger than the separation between the initially degenerate sublevels.

In a rotating condensate, for a sufficiently large rotation rate, there appear singularities called vortices, towards the center of which the particle density gradually vanishes and around which the phase of the macroscopic wave function winds by multiples of 2π. These vortices carry angular momentum which is quantized in units of $\hbar$. The occurrence of vortices in a superfluid is very similar to the piercing of a type-II superconductor by magnetic flux lines above a certain magnetic field called the lower critical field. By comparing the number of particles N to the number of vortices N_v, one can identify several rotation regimes in each of which the governing physics is different. If the filling factor $\nu = N/N_v$ is much larger than 1, then the system is said to be in the mean-field regime. For low rotation rates (but sufficiently high to create a vortex) several vortices appear in the condensate, and the treatment of this case depends on the construction of an appropriate Gross-Pitaevskii energy functional [15]. For larger rotation rates approaching the transverse trapping frequency, the system can still be described by a macroscopic wave function. As the rotation frequency increases the spatial extent of the gas also increases. At a point where both the interaction energy and the chemical potential become much smaller than the separation between the lowest and first excited (single particle) Landau levels, the macroscopic wave function can be written as a linear combination of the lowest Landau level (LLL) wave functions and has the general form as $\psi(z) = \exp(-|z|^2/2a_\perp^2)\prod_{m=1}^{n}(z - z_m)$, where $z = x + iy$, $a_\perp = \sqrt{\hbar/m\omega_\perp}$, and z_m are the n complex zeros of the wave function. This form also naturally describes the vortex structure since the phase of the wave function winds by 2π around each and every z_m. By taking z_m as variational parameters, one can then minimize the energy given by the Gross-Pitaevskii energy functional [16]. The result is a triangular lattice of vortices, which is the cold-atom analogue of the Abrikosov vortex lattice appearing in type-II superconductors [17]. As the rotation frequency further increases, the vortex lattice starts to melt [18]. This regime corresponds to $\nu \sim 6 - 10$. In the ultra-fast rotation limit, where the number of vortices per atom may be larger than one ($\nu = N/N_v < 1$), one has to deal with a strongly-correlated many-body phenomenon, which is intimately connected to the fractional quantum Hall (FQH) physics [19, 20, 21].

In a cold-atom system, rotation can be induced by applying an optical or magnetic stirring potential to the trapped condensate [22, 23]. However, due to the instability of the center-of-mass motion of the atom cloud occurring for fast rotation rates, one has to use other techniques to reach that limit. These techniques include an evaporative process in which atoms carrying less than average angular momentum are made to leave the system [24, 25] and the application of a quartic trapping potential in addition to the quadratic one [26]. Another method to reach fast rotation limit is to superimpose an optical lattice potential, which co-rotates with the condensate [27]. For a deep enough lattice, vortices may be pinned in or between the lattice sites, and structural phase transitions (e.g. from the usual triangular one to a square lattice) can be observed [28]. There are various methods to create a rotating periodic structure. One of them is to shine laser light on a rotating mask and then focus the passing light onto the condensate [27]. Another possible scheme is to use acousto-optic modulators which change the direction of counter-propagating laser beams continually and then again focus the beams through lenses [29, 30].

Fast rotating optical lattices promise huge artificial magnetic fluxes which are beyond the reach of conventional condensed matter experiments done with real crystals and magnetic fields. They thus provide the relevant setting for the study of various phenomena associated with large fluxes such as the lattice quantum Hall physics and the appearance of a single-particle fractal energy spectrum called the Hofstadter butterfly [31], which also has a bearing on the corresponding many-particle system. The basic Hamiltonian on which we will focus from now on is the Hamiltonian for a harmonically trapped particle in the frame of a rotating optical lattice (ROL) given by

$$H_{ROL} = \frac{(\mathbf{p}_\perp - m\Omega\hat{\mathbf{z}} \times \mathbf{r})^2}{2m} + V_0[\sin^2(kx) + \sin^2(ky)] + \frac{1}{2}m(\omega_\perp^2 - \Omega^2)(x^2 + y^2). \tag{1.14}$$

We will examine the energy spectrum of this Hamiltonian and some related quantities (e.g. Hall conductance) under certain approximations. For instance the lattice structure will be accounted for by the tight-binding approach. Magnetic field will show up in the tight-binding Hamiltonian through Peierls substitution. The residual trapping potential will either be assumed to vanish identically or be treated in the local density approximation. We will also generalize the Hamiltonian (1.14) for bosonic and fermionic many-body systems and look for ground state properties using an order-parameter approach.

As a final remark, we emphasize that, although it is conceptually simple, rotation is not the only or the best method to create an artificial magnetic field. There is a myriad of proposals to realize artificial gauge fields, which basically involve the usage of atom-light interactions and spatially varying atomic sublevels in order to employ a Berry phase effect for atoms or put simply, to impart the necessary momentum to them as if they were receiving the same momentum kick as charged particles receive in a magnetic field [32, 33, 34, 35, 36, 37, 38, 39, 40].

1.4 Single-particle Spectrum in a Rotating Optical Lattice

In this section, we will examine the single-particle spectrum in a lattice under an effective magnetic field for the lowest (s) band. The discussion of rotational effects on the first excited (p) band will be deferred to the next chapter. The interesting thing about studying this old problem [41, 42, 43, 44, 45, 46, 31] in the cold-atom context is that due to the adjustable parameters of cold-atom systems it has become feasible to observe the previously predicted spectrum and investigate its bearings on a number of other measurable properties such as the quantized Hall conductance. The implication of the single-particle spectrum on many-particle systems is also another important subject to quest for. The principal difficulty with solid-state systems is that the observation of many interesting effects involving magnetic field requires very huge field magnitudes. The main parameter that we will be interested in is the number of magnetic flux quanta per unit cell (plaquette) of the lattice $\phi = \Phi/\phi_0$, where $\Phi = Ba^2$ is the magnetic flux per plaquette and $\phi_0 = h/e = 4.14 \times 10^{-15}\mathrm{Wb}$ is the flux quantum ($1\mathrm{Wb} = 1\mathrm{Tesla} \times \mathrm{m}^2$). The phenomena that we are going to examine in subsequent chapters will appear when ϕ is an appreciable fraction of 1. For a value of, say, $\phi = 1$, the required magnetic field in a real crystal for which the lattice spacing a is about a few Å is of the order of 10^5 Tesla. On the other hand, the highest continuous magnetic field available nowadays is around only 50 Tesla [47]. So there is no prospect of reaching $\phi \sim 1$ regime with a conventional solid-state setup. One possible way to circumvent this difficulty is to use a synthetic lattice with larger lattice spacing. Indeed, in some experiments super-lattice structures have been used to study the splitting of Landau levels for sufficiently high field strengths under a periodic potential [48]; however, the tight-binding regime (and also the strong magnetic field limit) has never been experimentally realized. In a cold-atom setup, such a restriction on attaining high magnetic fluxes can be removed. Consider a rotating optical lattice, for instance, where ϕ can be linked to the rotation frequency Ω as $\phi = 2ma^2\Omega/h$. For a typical experiment done with ^{40}K atoms in a lattice with lattice spacing $a = 400$ nm, Ω has to be around 10 KHz in order to yield $\phi = 1/3$, which is not so high a frequency to reach.

We now turn to a general consideration of the single-particle physics in a periodic potential under a uniform magnetic field. Translational symmetry of the lattice is broken in a magnetic field. However, for a uniform magnetic field, a change of origin of the vector potential due to translation does not alter the physical situation and there should exist a proper set of translation operators, which differ from the field-free ones only by phase factors, that commute with the Hamiltonian $H = [\mathbf{p} - e\mathbf{A}(\mathbf{r})]^2/2m + V(\mathbf{r})$ [49, 50]. The magnetic translation operators for a uniform magnetic field can formally be constructed by investigating the Schrödinger equation for the system shifted by a lattice vector $\mathbf{a} = a(n_1\hat{\mathbf{x}} + n_2\hat{\mathbf{y}})$:

$$\left\{\frac{[\mathbf{p} - e\mathbf{A}(\mathbf{r}+\mathbf{a})]^2}{2m} + V(\mathbf{r})\right\}\psi(\mathbf{r}+\mathbf{a}) = E\psi(\mathbf{r}+\mathbf{a}), \tag{1.15}$$

where the periodicity of the lattice dictated $V(\mathbf{r}+\mathbf{a}) = V(\mathbf{r})$. The change of origin of the vector potential, which does not change the magnetic field, can be seen as a gauge transformation: $\mathbf{A}(\mathbf{r}+\mathbf{a}) = \mathbf{A}(\mathbf{r}) + \nabla f(\mathbf{r})$. Then, if one wishes to write Eq. (1.15) in terms of $\mathbf{A}(\mathbf{r})$ again, the wave functions should also transform by acquiring a phase factor of $\exp(-ief(\mathbf{r})/\hbar)$, which turns Eq. (1.15) into

$$\left\{\frac{[\mathbf{p} - e\mathbf{A}(\mathbf{r})]^2}{2m} + V(\mathbf{r})\right\}e^{-ief/\hbar}\psi(\mathbf{r}+\mathbf{a}) = Ee^{-ief/\hbar}\psi(\mathbf{r}+\mathbf{a}). \tag{1.16}$$

For a uniform magnetic field along $\hat{\mathbf{z}}$, $\mathbf{A}(\mathbf{r})$ has to be a linear function of x and y. Then $\nabla f(\mathbf{r}) = \mathbf{A}(\mathbf{r}+\mathbf{a}) - \mathbf{A}(\mathbf{r}) \equiv \Delta\mathbf{A}$ cannot depend on $\mathbf{r}$ and $f(\mathbf{r})$ simply becomes $\Delta\mathbf{A}\cdot\mathbf{r}$. This means that $e^{-ie\Delta\mathbf{A}\cdot\mathbf{r}/\hbar}\psi(\mathbf{r}+\mathbf{a})$ is a common eigenstate of H and an operator $T_{\mathbf{a}}$ ($[H, T_{\mathbf{a}}] = 0$), which we will call the magnetic translation operator, whose action on a state $\psi(\mathbf{r})$ is given by $T_{\mathbf{a}}\psi(\mathbf{r}) = e^{-ie\Delta\mathbf{A}\cdot\mathbf{r}/\hbar}\psi(\mathbf{r}+\mathbf{a})$. In this form, it is clear that the magnetic translation operator can be constructed from the usual translation operator by multiplying it with an appropriate phase factor, as expected. Throughout this work we will mostly use a specific form of the Landau gauge given by $\mathbf{A} = Bx\hat{\mathbf{y}}$. It is just a matter of convenience and it is possible to switch to another gauge through a simple gauge transformation. For instance, this gauge is related to the other form of the Landau gauge as $-By\hat{\mathbf{x}} = Bx\hat{\mathbf{y}} - \nabla(Bxy)$ and to the symmetric gauge via $B\hat{\mathbf{z}} \times \hat{\mathbf{r}}/2 = Bx\hat{\mathbf{y}} - \nabla(Bxy/2)$. Let us explicitly write these translation operators for a translation of one lattice spacing in each direction:

$$T_{a\hat{\mathbf{x}}} = e^{-i2\pi\phi y/a}e^{iap_x/\hbar}, \tag{1.17}$$

$$T_{a\hat{\mathbf{y}}} = e^{iap_y/\hbar}. \tag{1.18}$$

An important feature of these operators is that they do not commute with each other. Instead, they obey the following relation:

$$T_{a\hat{\mathbf{x}}}T_{a\hat{\mathbf{y}}} = e^{i2\pi\phi}T_{a\hat{\mathbf{y}}}T_{a\hat{\mathbf{x}}}. \tag{1.19}$$

For general magnetic translation operators $T_{\hat{\mathbf{a}}_1}$ and $T_{\hat{\mathbf{a}}_2}$ in an arbitrary lattice geometry, the phase factor in this relation can be generalized to be $\exp(ie\oint \mathbf{A}\cdot d\mathbf{r}/\hbar)$, $\oint \mathbf{A}\cdot d\mathbf{r}$ being the flux passing through the parallelogram whose sides are given by $\mathbf{a}_1$ and $\mathbf{a}_2$. If this flux is an integer multiple of the flux quantum ϕ_0, then $[T_{\hat{\mathbf{a}}_1}, T_{\hat{\mathbf{a}}_2}] = 0$. When ϕ is a rational number p/q, p and q being relatively prime integers, the operators $T_{a\hat{\mathbf{y}}}$ and $T_{qa\hat{\mathbf{x}}}$ of our square geometry commute as can be seen by repeatedly applying $T_{a\hat{\mathbf{x}}}$ onto Eq. (1.19) $(q-1)$ times from the left. Each change of order between $T_{a\hat{\mathbf{y}}}$ and $T_{a\hat{\mathbf{x}}}$ will bring the phase factor $\exp(i2\pi\phi)$ yielding a total of $\exp(i2\pi p) = 1$. Thus, the number of enclosed flux quanta in this $1 \times q$ rectangle is p, and we will refer to this unit cell as the magnetic super-cell. We now have a mutually commuting set of three operators, namely, H, $T_{a\hat{\mathbf{y}}}$, and $T_{qa\hat{\mathbf{x}}}$ in the lattice and this enables us to employ the magnetic version of Bloch's theorem for the common eigenstate of these operators, which we will denote by $\psi_{n,\mathbf{k}}(\mathbf{r})$, n being the band index and $\mathbf{k} = (k_x, k_y)$. One may also assume that the system is finite with $L_1 = sq$ (s is an integer) sites along the x direction and L_2 sites along the y direction, and impose periodic boundary conditions $\psi_{n,\mathbf{k}}(\mathbf{r}) = \psi_{n,\mathbf{k}}(\mathbf{r} + L_1 a\hat{\mathbf{x}}) = \psi_{n,\mathbf{k}}(\mathbf{r} + L_2 a\hat{\mathbf{y}})$, which will restrict k_x and k_y to discrete values. In the limit of an infinite system, k_x and k_y will be continuous. Using Bloch's theorem, we get the following eigenvalue equations

$$H\psi_{n,\mathbf{k}}(\mathbf{r}) = \epsilon_{n,\mathbf{k}}\psi_{n,\mathbf{k}}(\mathbf{r}), \tag{1.20}$$

$$T_{qa\hat{\mathbf{x}}}\psi_{n,\mathbf{k}}(\mathbf{r}) = e^{iqk_x a}\psi_{n,\mathbf{k}}(\mathbf{r}), \tag{1.21}$$

$$T_{a\hat{\mathbf{y}}}\psi_{n,\mathbf{k}}(\mathbf{r}) = e^{ik_y a}\psi_{n,\mathbf{k}}(\mathbf{r}), \tag{1.22}$$

where $k_x \subset [-\pi/qa, \pi/qa)$ and $k_y \subset [-\pi/a, \pi/a)$. This region of $\mathbf{k}$ space is usually called the magnetic Brillouin zone (MBZ). The reduction of the field-free Brillouin zone in the k_x direction by a factor of q is due to the enlargement of real-space unit cell in the x direction by the same factor. There is also another

q-fold degeneracy in the k_y direction, which will be important in our discussion of BCS type of fermion-pairing. In the end, the energy, which depends on k_x and k_y, should not be affected by our choice of gauge and it has to remain the same if we interchange k_x and k_y. To see this degeneracy in the k_y direction, it suffices to observe that $T_{la\hat{\mathbf{x}}}$ with $l = 1, \ldots, q-1$ is an eigenstate of both H and $T_{a\hat{\mathbf{y}}}$:

$$\begin{aligned} H[T_{la\hat{\mathbf{x}}}\psi_{n,\mathbf{k}}(\mathbf{r})] &= \epsilon_{n,\mathbf{k}}[T_{la\hat{\mathbf{x}}}\psi_{n,\mathbf{k}}(\mathbf{r})], && (1.23) \\ T_{a\hat{\mathbf{y}}}[T_{la\hat{\mathbf{x}}}\psi_{n,\mathbf{k}}(\mathbf{r})] &= e^{i(k_y a + 2\pi l p/q)}[T_{la\hat{\mathbf{x}}}\psi_{n,\mathbf{k}}(\mathbf{r})], && (1.24) \end{aligned}$$

which lead to the following properties [51, 50]

$$\begin{aligned} \psi_{n,\mathbf{k}}(\mathbf{r} + la\hat{\mathbf{x}}) &\propto \psi_{n,\mathbf{k}+2\pi lp/(qa)\hat{\mathbf{y}}}(\mathbf{r}), \\ \epsilon_{n,\mathbf{k}} &= \epsilon_{n,\mathbf{k}+2\pi lp/(qa)\hat{\mathbf{y}}}. && (1.25) \end{aligned}$$

Fig. 1.2 shows this three-fold degeneracy for $\phi = 1/3$ ($p = 1$, $q = 3$). Also shown is the splitting of the field-free Bloch band into three magnetic bands. In what follows, we direct our attention to the calculation of the energy spectrum for arbitrary ϕ in the tight-binding limit.

In the presence of a magnetic field, the simple zero-field tight-binding bands split in a nontrivial way, as verified by first-principle numerical calculations [52, 53]. However, it is highly desirable to find an effective Hamiltonian description in order to avoid heavy numerical calculations by adapting the known zero-field results to arbitrary field configurations with relative ease. One such method simple enough in respect of its prescription is the so-called Peierls substitution [41], the validity of which is verified to second order in the magnetic field for a single non-degenerate band [49]. If one knows the zero-field dispersion relation $E(\mathbf{k})$, in order to find the modified energy spectrum, one simply has to change $\mathbf{k}$ with the operator $(\mathbf{p} - e\mathbf{A})/\hbar$ making an effective Hamiltonian out of the zero-field energy spectrum. For higher field strengths, or rather an arbitrary field strength, it can also be proved that there exists an operator function

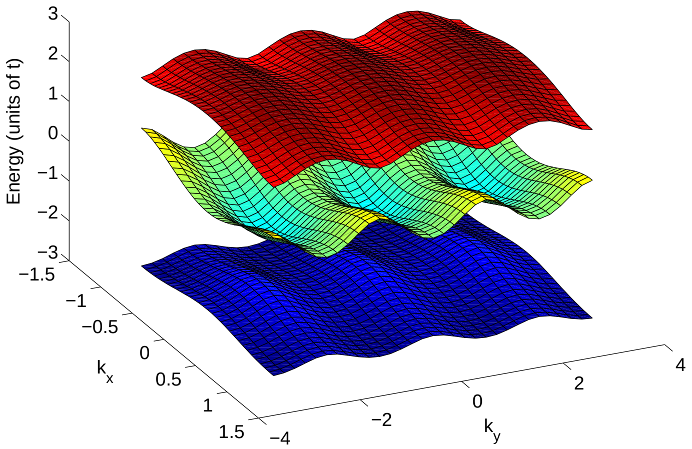

Figure 1.2: Energy spectrum for $\phi = 1/3$ ($p = 1$, $q = 3$). A single Bloch band is divided into $q = 3$ magnetic bands. Note the three-fold degeneracy in the k_y direction.

$W[(\mathbf{p} - e\mathbf{A})/\hbar]$ with the property that in the limit of vanishing magnetic field, $W(\mathbf{k})$ goes to $E(\mathbf{k})$. Again, in the tight-binding limit we will consider, we can plausibly argue that if the coefficients $W(\mathbf{R}_i)$ of the Fourier representation of $W(\mathbf{k})$ are negligible beyond nearest neighbors whenever $E(\mathbf{R}_i)$ are, then $W(\mathbf{k})$ can be represented by $E(\mathbf{k})$. With this assumption, we proceed to make the Peierls substitution in the lowest tight-binding (s) band, which has the form $E(\mathbf{k}) = -2t[\cos(k_x a) + \cos(k_y a)]$ and obtain the following single band effective Hamiltonian in a magnetic field [31]

$$H_0 = -t(e^{iap_x/\hbar} + e^{-iap_x/\hbar} + e^{iap_y/\hbar}e^{i2\pi\phi x/a} + e^{-iap_y/\hbar}e^{-i2\pi\phi x/a}), \tag{1.26}$$

where we have used the Landau gauge $\mathbf{A} = Bx\hat{\mathbf{y}}$ and turned cosine functions into exponentials obtaining translation operators. In this form, we observe that translations along the y direction are multiplied by phases which depend on the x coordinate. In the ensuing eigenvalue equation, the coefficients do not depend on y, so one can assume a plane wave behavior for the wave function in the y direction and the equation is thus reduced to one dimension. At this point, it is appropriate to introduce a second quantized notation, which will allow us to easily generalize the single-particle results to the many-body case.

So we write the single-particle effective Hamiltonian as

$$H_0 = -t \sum_{\langle i,j \rangle} a_i^\dagger a_j e^{iA_{ij}}, \tag{1.27}$$

where a_i ($a_i^\dagger$) is the bosonic annihilation (creation) operator at site i and $\langle i, j \rangle$ denotes summation over nearest neighbors. Magnetic field affects the Hamiltonian through A_{ij} which is equal to $2\pi m\phi(i_y - j_y)$, if $i_x = j_x = ma$ and is 0 otherwise. It can be shown that the magnetic translation operators given by Eqs. (1.17) and (1.18) commute also with this effective Hamiltonian. In this notation our ansatz state ket will be $|\psi\rangle = |p_y\rangle \sum_m c_m |m\rangle$, where $|p_y\rangle$ is the momentum eigenket ($\langle \mathbf{r}|p_y\rangle = e^{ik_y y}$) and $|m\rangle$ represents a basis ket which is localized along the x axis. If we operate on this ket with the Hamiltonian (1.27), we get the following difference equation (also known as Harper's equation) for the expansion coefficients c_m:

$$c_{m+1} + c_{m-1} + 2\cos(2\pi m\phi - k_y a)c_m = \frac{E}{t} c_m. \tag{1.28}$$

If ϕ is a rational number p/q, the wave function satisfies the Bloch condition $c_{m+q} = \exp(iqk_x a)c_m$ as a result of the symmetry under q-site translation in the x direction. The allowed energies are then found as the eigenvalues of the $q \times q$ tridiagonal matrix:

$$\mathbb{A}_q(k_x, k_y) = \begin{pmatrix} . & \ddots & . & . & e^{-iqk_x a} \\ \ddots & \ddots & 1 & . & . \\ . & 1 & 2\cos(2\pi m\phi - k_y a) & 1 & . \\ . & . & 1 & \ddots & \ddots \\ e^{iqk_x a} & . & . & \ddots & . \end{pmatrix}. \tag{1.29}$$

We call the matrix formed by setting $k_x = k_y = 0$ in (1.29) $\mathbb{A}_q$. The maximum eigenvalue of $\mathbb{A}_q$ yields the maximum energy of the system for a given ϕ. We define this energy as $f(\phi)$, which is a continuous but not differentiable function owing to the fractal nature of the energy spectrum (Fig. 1.3). To prove that the maximum energy is obtained from $\mathbb{A}_q$, we investigate the characteristic equation for the matrix (1.29), which is of the following form:

$$\left(\frac{E}{t}\right)^q + \sum_{n=0}^{q-1} a_n \left(\frac{E}{t}\right)^n - 2\cos(qk_x a) - 2\cos(qk_y a) = 0. \tag{1.30}$$

This equation is most easily obtained by first considering the k_x dependent term, which is easier to be determined and then using a duality argument which states that the energy should depend on k_x and k_y in the same way. Two pairs of (k_x, k_y), namely $(0, 0)$ and $(\pi/qa, \pi/qa)$ are sufficient to determine the extremal values of the energy (band edges) [54]. The $(0, 0)$ pair gives a smaller value for the k_x and k_y dependent terms. Since the E dependent part of (1.30) increases monotonically after a sufficiently large E, the greatest root is always obtained from the $(0, 0)$ pair [55]. Moreover, this pair yields the minimum eigenvalue as well since it is just the negative of the maximum eigenvalue as can be observed from Fig. 1.3 (more generally if E is a solution, then $-E$ is also a solution, which is a consequence of the square lattice being bipartite). Another remarkable feature of this self-similar energy spectrum (frequently called the Hofstadter butterfly) is that there is a reflection symmetry with respect to the $\phi = 1/2$ line. That is, the spectrum is the same for $\phi = p/q$ and $\phi = (q - p)/q$. This is because $\phi = (q - p)/q = 1 - p/q$ has to yield the same spectrum as $\phi = -p/q$ since adding or subtracting an integer number of flux quantum should not change the physics [a fact which can formally be deduced from the difference equation (1.30)]. A minus sign in front of $\phi = -p/q$ simply means that the field direction is reversed, which again has no consequence on the energy spectrum.

We will repeatedly encounter the signatures of this single-particle Hofstadter spectrum on all of the phenomena we are going to investigate in succeeding chapters, which include both noninteracting and interacting systems of bosons and fermions.

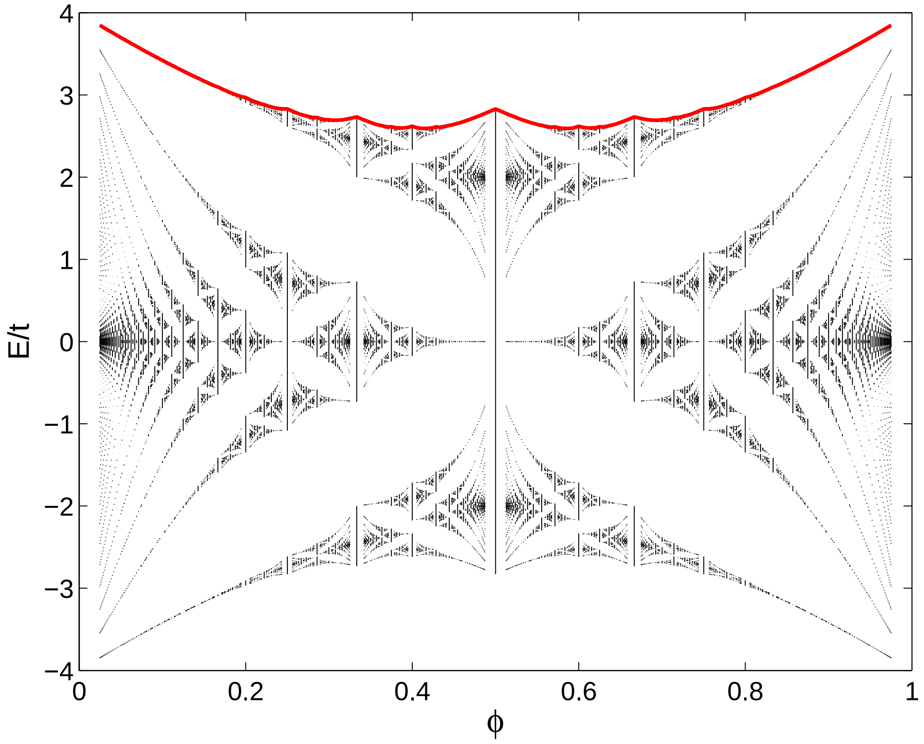

Figure 1.3: Energy spectrum as a function of the number of magnetic flux quanta per plaquette $\phi = p/q$. Maximum energy of the spectrum $f(\phi)$ is shown by the red solid line. This value is calculated as the maximum eigenvalue of the matrix $\mathbb{A}_q = \mathbb{A}_q(k_x = 0, k_y = 0)$ [Eq. (1.29)]. All fractions up to 39/40 are included.

Chapter 2

p Band in a Rotating Optical Lattice

An exciting development in cold atom physics has been the realization that higher bands in an optical lattice are also experimentally accessible [56, 57]. For a system of fermions the first excited band, i.e. the p band, can be accessed trivially by continuing to add particles after the s band is filled completely; for bosons the relaxation time in the p band is surprisingly long enough to allow experimental access to pure p-band physics. A natural question to ask about these systems is how the particles in the p band respond to the effective magnetic field created by rotation. One can imagine the already rich physics of the p band [58, 59, 60, 61, 62, 63, 64], which contains surprises such as Bose condensation at nonzero momentum, to be strongly affected by the magnetic field, as both the orbital order within each lattice site and the hopping between different lattice sites will be modified. Beyond the single-particle physics, it is not clear how the various many-particle phases, such as orbitally ordered Mott insulators [65, 66, 67, 68], will be affected by rotation.

The theoretical investigation of such effects requires a consistent method of incorporating the phases generated by the magnetic field into the lattice Hamiltonian. The magnetic fine structure of the lowest (s) band (which is a single non-degenerate band, see Sec. 1.4) is very well described by the Peierls substitution, the accuracy of which was checked by numerical solutions of the Schrödinger equation [53]. However, as for degenerate bands (of which the p band is the simplest example), the conjecture was that "wherever the unperturbed Bloch bands touch or overlap, it is not possible to obtain the magnetic sub-structure by semiclassical methods, even approximately, by means of a universal rule for the whole Brillouin zone" [52, 53]. Here, we generalize the Peierls substitution procedure to the p band, and obtain an effective Hamiltonian for the p band of the rotating optical lattice. We will show that after an appropriate diagonalization in $\mathbf{k}$ space, which assumes temporarily that only the on-site energies are affected by the degeneracy lifting field, Peierls substitution is still a good option to obtain the detailed magnetic fine structure. Our method should in principle be applicable to other degenerate bands and it provides us with a means to examine inter-particle interactions. The following discussion is based on the material of Ref. [69].

2.1 Model

Our approach will be to first cast the single-particle Hamiltonian (1.14) (after omitting the residual trapping term) into a second quantized form which includes the anisotropic hopping between nearest neighbor sites, the on-site zero point energies, and also the shift caused by rotation. Not only do we expect the hopping between lattice sites to be affected, as it was for the s band, but also the on-site energies to be modified. However, since the hopping and on-site Hamiltonians do not commute, a common transformation that accounts for both modifications cannot be found. To overcome this difficulty, we temporarily assume that the hopping amplitudes are not affected by the effective magnetic field and the only change is in the on-site energies. Our expectation is that in this way we will obtain two non-degenerate bands to which we can apply Peierls substitution separately. This procedure is rather *ad hoc* the validity of which is later checked through a comparison with the first-principles results presented previously [53] and reproduced here partially.

We proceed with considering the following p-band tight-binding Hamiltonian (the energy spectrum of which is measured relative to the center of the tight-binding s band) including the on-site zero-point energies and the rotation term ($-\Omega L_z$) [58, 64]

$$\begin{aligned} H &= \sum_{\mathbf{R},\mu,\nu} t_{\mu\nu}(b^\dagger_{\mu,\mathbf{R}+a\mathbf{e}_\nu} b_{\mu\mathbf{R}} + \text{h.c.}) + \hbar\omega \sum_{\mathbf{R},\mu} b^\dagger_{\mu\mathbf{R}} b_{\mu\mathbf{R}} \\ &+ i\hbar\Omega \sum_{\mathbf{R}} (b^\dagger_{x\mathbf{R}} b_{y\mathbf{R}} - b^\dagger_{y\mathbf{R}} b_{x\mathbf{R}}), \end{aligned} \tag{2.1}$$

where the summation is over all lattice sites $\mathbf{R}$ and band indices $\mu = x, y$ (since the problem is two-dimensional, p_z orbital will not be considered). As usual, $b^\dagger_{\mu\mathbf{R}}$ ($b_{\mu\mathbf{R}}$) is the creation (annihilation) operator for a particle in the p_μ band at lattice site $\mathbf{R}$, $\mathbf{e}_\nu$ is the unit vector along the ν direction, ω is the frequency of the isotropic harmonic oscillator potential which models the lattice potential around its minima, and $t_{\mu\nu}$ is the anisotropic hopping amplitude. The explicit expression for $t_{\mu\nu}$ (in the absence of rotation) is

$$t_{\mu\nu} = \int w^*_{p_\mu}(\mathbf{r})[\frac{-\hbar^2\nabla^2}{2m} + V(\mathbf{r})] w_{p_\mu}(\mathbf{r} + a\mathbf{e}_\nu) d\mathbf{r} \equiv t_\parallel \delta_{\mu\nu} - (1 - \delta_{\mu\nu}) t_\perp, \tag{2.2}$$

where $V(\mathbf{r})$ is the periodic lattice potential and $w_{p_\mu}(\mathbf{r})$ is the localized Wannier function corresponding to the p_μ band. When we approximate the lattice potential by a harmonic oscillator around a minimum, these can be expressed as a product of harmonic oscillator eigenfunctions, *i.e.* $w_{p_x}(\mathbf{r}) = u_1(x)u_0(y)$ and $w_{p_y}(\mathbf{r}) = u_0(x)u_1(y)$, $u_n(x)$ being the nth harmonic oscillator eigenfunction. $t_\parallel$ is the hopping amplitude between two neighboring p orbitals aligned along the orbital orientation and $t_\perp$ is the amplitude when the orbitals are oriented transversely with respect to the line connecting them. Both amplitudes are defined to be positive and $t_\parallel \gg t_\perp$ due to larger overlap. Since the lattice potential is separable in x and y coordinates, $t_\parallel$ and $t_\perp$ indeed have simple expressions in reference to the one-dimensional problem. $t_\perp$ and $t_\parallel$ are one quarter of the widths of the lowest and next lowest bands for $V = V_0 \sin^2(kx)$, respectively. By solving the Schrödinger equation numerically, we find $t_\perp = 0.0025E_R$ and $t_\parallel = 0.0603E_R$ for $V_0 = 20E_R$ [recall that $E_R = \hbar^2k^2/2m = h^2/8ma^2$ and since $\phi = 2ma^2\Omega/h$, the rotational energy is $\hbar\Omega = (2\phi/\pi)E_R$].

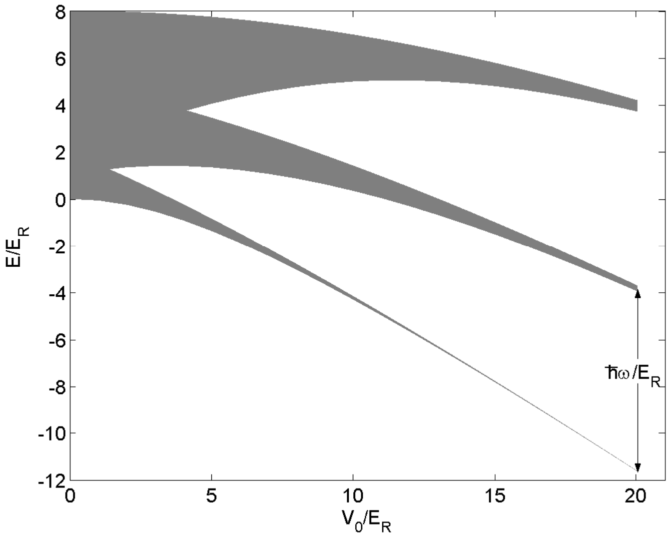

Figure 2.1: Lowest three bands for the two dimensional sinusoidal lattice potential. The energy difference between the lowest two bands (s and degenerate p levels) (measured from the band centers) is $\hbar\omega$ within the harmonic oscillator approximation for the potential minima, ω being the oscillator frequency. For $V_0 = 20E_R$, $\hbar\omega = 7.7739E_R$.

The on-site zero-point energy $\hbar\omega$ also has the simple interpretation of being the energy difference between s and p levels (bearing in mind the harmonic description, see Fig. 2.1).

2.2 Peierls Substitution and Magnetic Fine Structure

We perform a Fourier transformation on the Hamiltonian [Eq. (2.1)] as a preliminary for diagonalization in momentum space. The transformed Hamiltonian is

$$H=\sum_{\mathbf{k}}\left[(\epsilon_{x\mathbf{k}}+\hbar\omega)b^\dagger_{x\mathbf{k}}b_{x\mathbf{k}}+(\epsilon_{y\mathbf{k}}+\hbar\omega)b^\dagger_{y\mathbf{k}}b_{y\mathbf{k}}+i\hbar\Omega(b^\dagger_{x\mathbf{k}}b_{y\mathbf{k}}-b^\dagger_{y\mathbf{k}}b_{x\mathbf{k}})\right], \quad (2.3)$$

where $\epsilon_{\mu\mathbf{k}} = 2\sum_\nu t_{\mu\nu}\cos(k_\nu a)$. Since the Hamiltonian is bilinear in creation and annihilation operators, it is diagonalizable by a Bogoliubov transformation.

Defining $f_{1\mathbf{k}} \equiv \epsilon_{x\mathbf{k}} + \hbar\omega$ and $f_{2\mathbf{k}} \equiv \epsilon_{y\mathbf{k}} + \hbar\omega$, we observe that the Hamiltonian is diagonalized in $\mathbf{k}$ space by the following transformation:

$$\alpha_{\mathbf{k}} = \frac{1}{\sqrt{2}}[(\cos\theta_{\mathbf{k}} + \sin\theta_{\mathbf{k}})b_{x\mathbf{k}} + i(\cos\theta_{\mathbf{k}} - \sin\theta_{\mathbf{k}})b_{y\mathbf{k}}]$$

$$\beta_{\mathbf{k}} = \frac{1}{\sqrt{2}}[(\cos\theta_{\mathbf{k}} - \sin\theta_{\mathbf{k}})b_{x\mathbf{k}} - i(\cos\theta_{\mathbf{k}} + \sin\theta_{\mathbf{k}})b_{y\mathbf{k}}], \tag{2.4}$$

with

$$\begin{aligned}\cos 2\theta_{\mathbf{k}} &= \frac{1}{\sqrt{1+\left(\frac{f_{1\mathbf{k}}-f_{2\mathbf{k}}}{2\hbar\Omega}\right)^2}},\\ \sin 2\theta_{\mathbf{k}} &= \frac{f_{1\mathbf{k}}-f_{2\mathbf{k}}}{2\hbar\Omega}\frac{1}{\sqrt{1+\left(\frac{f_{1\mathbf{k}}-f_{2\mathbf{k}}}{2\hbar\Omega}\right)^2}}.\end{aligned}$$

The diagonal Hamiltonian has the form

$$H = \sum_{\mathbf{k}} [E_\alpha(\mathbf{k})\alpha^\dagger_{\mathbf{k}}\alpha_{\mathbf{k}} + E_\beta(\mathbf{k})\beta^\dagger_{\mathbf{k}}\beta_{\mathbf{k}}],$$

with

$$E_{\alpha,\beta}(\mathbf{k}) = \frac{f_{1\mathbf{k}}+f_{2\mathbf{k}}}{2} \pm \hbar\Omega\sqrt{1+\left(\frac{f_{1\mathbf{k}}-f_{2\mathbf{k}}}{2\hbar\Omega}\right)^2}, \tag{2.5}$$

where upper (lower) sign refers to α (β). From this point on, we can in principle apply Peierls substitution to the dispersion relation [Eq. (2.5)] in order to obtain an operator out of it, *i.e.* we change $\mathbf{k}$ to $(\mathbf{p} - e\mathbf{A})/\hbar$ using the Landau gauge $\mathbf{A} = Bx\hat{\mathbf{y}}$. However, the resulting Hamiltonian will be transparent only when expressed in terms of a power series

$$E_{\alpha,\beta}(\mathbf{k}) = \frac{f_{1\mathbf{k}}+f_{2\mathbf{k}}}{2} \pm \hbar\Omega\Big[1+\frac{1}{2}\Big(\frac{f_{1\mathbf{k}}-f_{2\mathbf{k}}}{2\hbar\Omega}\Big)^2 - \frac{1}{8}\Big(\frac{f_{1\mathbf{k}}-f_{2\mathbf{k}}}{2\hbar\Omega}\Big)^4 + ...\Big], \tag{2.6}$$

with the assumption that $|f_{1\mathbf{k}} - f_{2\mathbf{k}}|/2\hbar\Omega = |\cos(k_x a) - \cos(k_y a)|(t_\parallel + t_\perp)/\hbar\Omega$ is smaller than one. If $(t_\parallel + t_\perp)/\hbar\Omega$ is much smaller than one, terms of lower order in $(f_{1\mathbf{k}} - f_{2\mathbf{k}})/2\hbar\Omega$ will be more dominant and one needs to consider only few terms for a desired accuracy, instead of summing the whole series. Increasing accuracy is achieved by adding higher order terms. In a typical experimental condition, for instance, with $V_0 = 20E_R$ and $\hbar\Omega \sim E_R$, the ratio $(t_\parallel + t_\perp)/\hbar\Omega$

is ~ 0.063, so a first order approximation may be sufficient for the desired accuracy. Here, we give the results to second order in $(f_{1\mathbf{k}} - f_{2\mathbf{k}})/2\hbar\Omega$, for completeness. The approximate energy band functions, where we retain terms up to second order, are then

$$\begin{aligned} E_{\alpha,\beta}(\mathbf{k}) &= \frac{f_{1\mathbf{k}} + f_{2\mathbf{k}}}{2} \pm \hbar\Omega\Big[1 + \frac{1}{2}\Big(\frac{f_{1\mathbf{k}} - f_{2\mathbf{k}}}{2\hbar\Omega}\Big)^2\Big] \\ &= c_0^{\pm} + c_1[\cos(k_x a) + \cos(k_y a)] \\ &+ c_2^{\pm}[\cos^2(k_x a) + \cos^2(k_y a) - 2\cos(k_x a)\cos(k_y a)], \end{aligned} \tag{2.7}$$

where $c_0^{\pm} = \hbar(\omega \pm \Omega)$, $c_1 = t_{\parallel} - t_{\perp}$, and $c_2^{\pm} = \pm(t_{\parallel} + t_{\perp})^2/2\hbar\Omega$. After converting cosines into sums of exponentials and making the Peierls substitution we obtain discrete translation operators, which allow us to express the eigenvalue problem as a difference equation. Since translations along y are multiplied by phases depending on x in the Landau gauge, one should be careful in creating an operator from cross terms such as $\exp(ik_x a)\exp(ik_y a)$. The correct way of transforming should yield Hermitian operators and is obtained by symmetric combinations such as

$$e^{ik_x a}e^{ik_y a} \rightarrow \frac{e^{iap_x/\hbar}e^{ia(p_y - eBx)/\hbar} + e^{ia(p_y - eBx)/\hbar}e^{iap_x/\hbar}}{2}. \tag{2.8}$$

As it has been done for the s band, due to the translational invariance of the problem along the y direction, the y dependent part of the wave function will be taken to be a plane wave [31]

$$\psi(x, y) = e^{ik_y y} g(x). \tag{2.9}$$

Making the substitutions $x = na$ and $y = la$, n and l being integers, and acting the effective Hamiltonian $E_{\alpha,\beta}[(\mathbf{p} - eBx\hat{\mathbf{y}})/\hbar]$ on the wave function [Eq. (2.9)], we get the following difference equation

$$\begin{aligned} Eg(n) &= \Big[\frac{c_2^{\pm}}{2}\cos(4\pi n\phi - 2k_y a) + c_1\cos(2\pi n\phi - k_y a) + c_0^{\pm} + c_2^{\pm}\Big]g(n) \\ &+ \Big(\frac{c_1}{2} - \frac{c_2^{\pm}}{2}\{\cos(2\pi n\phi - k_y a) + \cos[2\pi(n+1)\phi - k_y a]\}\Big)g(n+1) \\ &+ \Big(\frac{c_1}{2} - \frac{c_2^{\pm}}{2}\{\cos(2\pi n\phi - k_y a) + \cos[2\pi(n-1)\phi - k_y a]\}\Big)g(n-1) \end{aligned}$$

$$+ \quad \frac{c_2^{\pm}}{4}[g(n+2)+g(n-2)], \tag{2.10}$$

where $c_0^{\pm}$, c_1, and $c_2^{\pm}$ were introduced following Eq. (2.7).

Again, when $\phi = p/q$, p and q being relatively prime integers, the difference equation [Eq. (2.10)] yields q equations together with the Bloch condition $g(n+q) = e^{ik_x qa} g(n)$. By diagonalizing the resulting $q \times q$ coefficient matrix for several k_x and k_y pairs, we obtain the energy eigenvalues which are plotted in Fig. 2.2 as a function of ϕ. We observe that each split band further divides into q subbands forming a pattern which has close resemblance to the Hofstadter butterfly. This result is in fact anticipated since $c_2^{\pm} = \pm(t_{\|} + t_{\perp})^2/2\hbar\Omega$ is much smaller than $c_1 = t_{\|} - t_{\perp}$ and if we simply neglect it as a first approximation, the energy band function [Eq. (2.7)] will just be that of the tight-binding s band, except that the difference $c_0^{+} - c_0^{-} = 2\hbar\Omega$ gives rise to increasing separation between the split p bands with increasing ϕ. Our approximation becomes poorer as ϕ (or Ω) becomes smaller since we require that $(t_{\|} + t_{\perp})/\hbar\Omega$ be small. This is apparent in Fig. 2.2 in which we highlight the region where two bands overlap. However, if we increase the lattice depth, which decreases the hopping amplitudes, we can increase the region of validity. Equivalently, we can say that our results should improve as ϕ increases. Another improvement option would be to consider a higher order expansion in translation operators, which models long-range hopping with yet smaller amplitudes.

To be able to judge the accuracy of the magnetic fine structure obtained by our method we compare it with a direct numerical solution of the Schrödinger equation, starting from the original Hamiltonian in the rotating frame (with the residual trapping term omitted) [Eq. (1.14)]. One method of numerical solution is to reduce the problem to a magnetic unit cell using magnetic translation symmetry and solve the two dimensional Schrödinger equation within this unit cell using finite difference methods. Unfortunately, the magnetic unit cell size increases with q, the denominator of the flux $\phi = p/q$, and the nontrivial boundary conditions required by magnetic translation symmetry makes this direct solution method computationally inefficient. Another, more efficient method, which was first developed by Zak [45], and then expanded on by

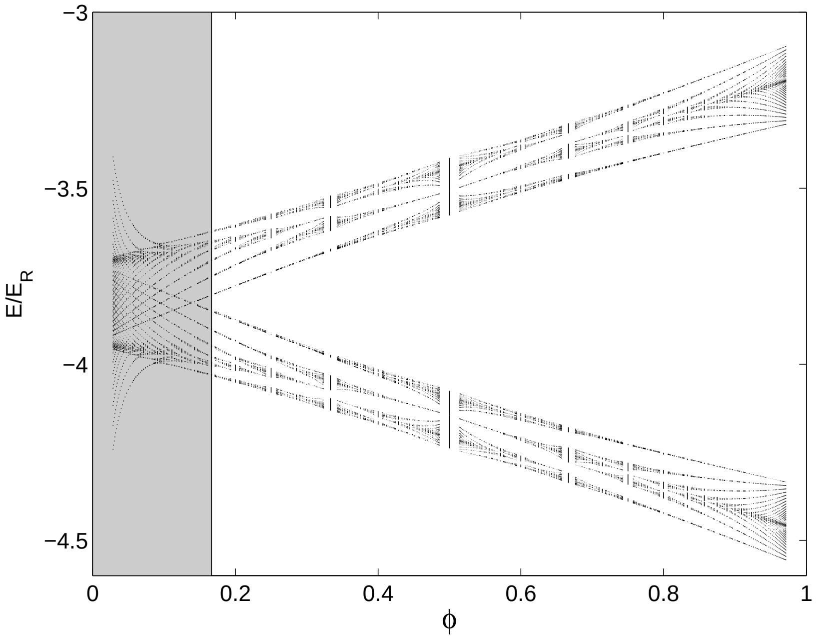

Figure 2.2: Magnetic fine structure of the p band for $V_0 = 20E_R$. Two-fold degenerate zero-field p band is split into two as $\phi = p/q$ grows. Each split band further has q subbands. Our approximation fails in the shaded region, corresponding to $\phi \lesssim 1/6$ (the nearest $\phi = 1/q$ to $1/5$, for which the spectrum is displayed in Fig. 2.3), where two bands overlap. This region can be made narrower if the lattice depth V_0 is increased.

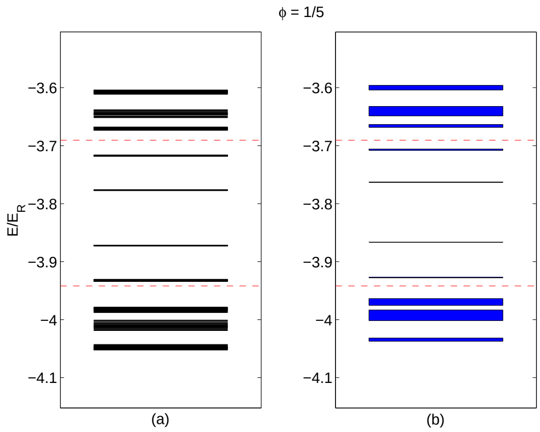

Figure 2.3: (a) Approximate energy levels, corresponding to $\phi = 1/5$, in our effective Hamiltonian approach. (b) Band diagram obtained through a first-principles calculation in which a truncated basis of harmonic oscillator wave functions is used. Dashed lines show the edges of the zero-field p band.

Obermair *et. al.* [52, 53], is to use magnetic translation symmetry to reduce the two dimensional Schrödinger equation to a set of p one-dimensional equations with nonlocal couplings. These equations can be handled with relative ease using a truncated basis of harmonic oscillator wave functions. Still, a numerical calculation is efficient only for pure cases with $\phi = 1/q$ and for small q values.

In Figs. 2.3 and 2.4, we compare our results with those obtained by a direct numerical calculation along the lines of Ref. [53].Calculations with the effective Hamiltonian are much faster and the results are as good as the direct numerical solution. For instance, in the case of $\phi = 1/5$ (Fig. 2.3) the agreement is already good, but if we increase ϕ to $1/3$ (Fig. 2.4), apart from a slight overall shift, we see that band gaps are also more faithfully reproduced.

2.3 Effective Hamiltonian

The computational efficiency of the effective Hamiltonian method for the single-particle problem is striking, but its real utility is that it can be used as a starting point to include interactions in the system. Interaction effects for the s band,

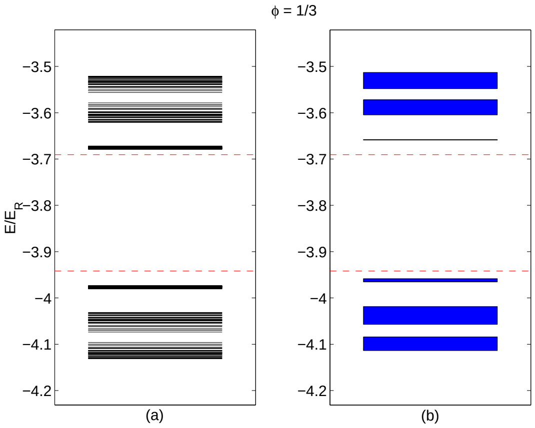

Figure 2.4: Energy levels for $\phi = 1/3$. (a) Results of the effective Hamiltonian approach. (b) First-principles band diagram. Our approximation is better compared to the case of $\phi = 1/5$, depicted in Fig. 2.3, in the sense that here band gaps are also more correctly captured, apart from a slight overall shift. Also shown, by dashed lines, are the edges of the zero-field p band.

starting from the Hamiltonian (1.27), will be investigated separately and more extensively in the next chapter. The results we obtained for the present p band case can be utilized to examine the case of many particles, if we first write the single-particle effective Hamiltonian in real space

$$
\begin{aligned}
H_{eff} &= \frac{1}{4}\sum_{\langle\langle\langle \mathbf{r},\mathbf{r}'\rangle\rangle\rangle} A_{\mathbf{r},\mathbf{r}'}(c_2^+\alpha_{\mathbf{r}}^\dagger\alpha_{\mathbf{r}'} + c_2^-\beta_{\mathbf{r}}^\dagger\beta_{\mathbf{r}'}) - \frac{1}{4}\sum_{\langle\langle \mathbf{r},\mathbf{r}'\rangle\rangle} B_{\mathbf{r},\mathbf{r}'}(c_2^+\alpha_{\mathbf{r}}^\dagger\alpha_{\mathbf{r}'} + c_2^-\beta_{\mathbf{r}}^\dagger\beta_{\mathbf{r}'}) \\
&+ \frac{c_1}{2}\sum_{\langle \mathbf{r},\mathbf{r}'\rangle} C_{\mathbf{r},\mathbf{r}'}(\alpha_{\mathbf{r}}^\dagger\alpha_{\mathbf{r}'} + \beta_{\mathbf{r}}^\dagger\beta_{\mathbf{r}'}) + \sum_{\mathbf{r}}[(c_0^+ + c_2^+)\alpha_{\mathbf{r}}^\dagger\alpha_{\mathbf{r}} + (c_0^- + c_2^-)\beta_{\mathbf{r}}^\dagger\beta_{\mathbf{r}}], \quad (2.11)
\end{aligned}
$$

$$
A_{\mathbf{r},\mathbf{r}'} = \begin{cases} e^{\pm i4\pi n\phi}, & \mathbf{r} \text{ and } \mathbf{r}' \text{ have } x = na \\ 1, & \text{otherwise.} \end{cases}
$$

$$
B_{\mathbf{r},\mathbf{r}'} = \begin{cases} e^{i2\pi(\pm n+1)\phi} + e^{\pm i2\pi n\phi}, & \mathbf{r} \text{ and } \mathbf{r}' \text{ on } y = -x \\ e^{i2\pi(\pm n-1)\phi} + e^{\pm i2\pi n\phi}, & \mathbf{r} \text{ and } \mathbf{r}' \text{ on } y = x \\ & (\mathbf{r} \text{ or } \mathbf{r}' \text{ has } x = na). \end{cases}
$$

$$C_{\mathbf{r},\mathbf{r}'} = \begin{cases} e^{\pm i2\pi n\phi}, & \mathbf{r} \text{ and } \mathbf{r}' \text{ have } x = na \\ 1, & \text{otherwise.} \end{cases}$$

Here, $\langle \mathbf{r}, \mathbf{r}' \rangle$ denotes summation over nearest neighbors in the square lattice (with separation a), $\langle\langle \mathbf{r}, \mathbf{r}' \rangle\rangle$ over next-nearest neighbors (with separation $\sqrt{2}a$), and $\langle\langle\langle \mathbf{r}, \mathbf{r}' \rangle\rangle\rangle$ over next-next-nearest neighbors (with separation $2a$); ± sign refers to the hopping direction. We note that the next-nearest and next-next-nearest coupling amplitudes turn out to be the same in our approximation. This effective Hamiltonian represents noninteracting particles occupying the p band of a square lattice under a particular magnetic flux ϕ. The connection between the new and old operators is made through the following definition

$$\begin{aligned} \alpha_{\mathbf{k}} &\equiv \cos\theta_{\mathbf{k}} b^{+}_{\mathbf{k}} + \sin\theta_{\mathbf{k}} b^{-}_{\mathbf{k}}, \\ \beta_{\mathbf{k}} &\equiv \cos\theta_{\mathbf{k}} b^{-}_{\mathbf{k}} - \sin\theta_{\mathbf{k}} b^{+}_{\mathbf{k}}, \end{aligned}$$

with $b^{\pm}_{\mathbf{k}} \equiv (b_{x\mathbf{k}} \pm i b_{y\mathbf{k}})/\sqrt{2}$. The operator $b^{+}_{\mathbf{k}}$ ($b^{-}_{\mathbf{k}}$) annihilates a particle with momentum $\hbar\mathbf{k}$ whose z component of angular momentum is $-\hbar$ ($\hbar$). To first order in $(t_{\parallel} + t_{\perp})/\hbar\Omega$, $\alpha_{\mathbf{k}}$ and $\beta_{\mathbf{k}}$ are of the following form

$$(\alpha, \beta)_{\mathbf{k}} = b^{\pm}_{\mathbf{k}} \pm \frac{t_{\parallel} + t_{\perp}}{2\hbar\Omega}(\cos k_x a - \cos k_y a) b^{\mp}_{\mathbf{k}},$$

where the upper (lower) sign refers to α (β). After expressing cosines as exponentials, we make the Peierls substitution, *i.e.* we change $\mathbf{k}$ to $\mathbf{k} - eBx\hat{\mathbf{y}}/\hbar$ in the coefficients of $b^{\pm}_{\mathbf{k}}$ and interpret the resulting factors $\exp(\pm i2\pi\phi x/a)$ as momentum translation operators whose action on a function of $\mathbf{k}$ is given by $\exp(\pm i2\pi\phi x/a) f(\mathbf{k}) = f(\mathbf{k} \mp 2\pi\phi\hat{\mathbf{x}}/a)$. Fourier transformation of these modified operators yields the real space operators as

$$(\alpha, \beta)_{n,l} = b^{\pm}_{n,l} \pm \frac{t_{\parallel} + t_{\perp}}{4\hbar\Omega}(b^{\mp}_{n+1,l} + b^{\mp}_{n-1,l} - e^{i2\pi\phi n} b^{\mp}_{n,l+1} - e^{-i2\pi\phi n} b^{\mp}_{n,l-1}), \quad (2.12)$$

where the indices (n, l) specify the x ($= na$) and y ($= la$) coordinates.

While we performed a second order expansion in the ratio of the hopping parameter $t_{\parallel}$ ($\gg t_{\perp}$) to $\hbar\Omega$, which is a small parameter for tight-binding lattices except in the limit of very slow rotation, it is instructive to display the effective

Hamiltonian to first order in $(t_{\parallel}+t_{\perp})/\hbar\Omega$ in terms of the original operators $b_{\mu\mathbf{r}}$:

$$\begin{aligned}
H_{eff} &= \frac{t_{\parallel}+t_{\perp}}{2}\sum_{\langle\mathbf{r},\mathbf{r}'\rangle}[C_{\mathbf{r},\mathbf{r}'}(b^{+}_{\mathbf{r}})^{\dagger}b^{-}_{\mathbf{r}'}(1-2\delta_{(\mathbf{r})_x(\mathbf{r}')_x})+\text{h.c.}]\\
&+ \frac{t_{\parallel}-t_{\perp}}{2}\sum_{\langle\mathbf{r},\mathbf{r}'\rangle}C_{\mathbf{r},\mathbf{r}'}[(b^{+}_{\mathbf{r}})^{\dagger}b^{+}_{\mathbf{r}'}+(b^{-}_{\mathbf{r}})^{\dagger}b^{-}_{\mathbf{r}'}]+\sum_{\mathbf{r}}[\hbar(\omega+\Omega)n^{+}_{\mathbf{r}}+\hbar(\omega-\Omega)n^{-}_{\mathbf{r}}]\\
&= \sum_{\mathbf{r},\mu,\nu}t_{\mu\nu}[b^{\dagger}_{\mu,\mathbf{r}+a\mathbf{e}_{\nu}}b_{\mu\mathbf{r}}\exp\left(ie\int_{\mathbf{r}}^{\mathbf{r}+a\mathbf{e}_{\nu}}\mathbf{A}\cdot d\mathbf{r}'/\hbar\right)+\text{h.c.}]\\
&+ \hbar\omega\sum_{\mathbf{r},\mu}b^{\dagger}_{\mu\mathbf{r}}b_{\mu\mathbf{r}}+i\hbar\Omega\sum_{\mathbf{r}}(b^{\dagger}_{x\mathbf{r}}b_{y\mathbf{r}}-b^{\dagger}_{y\mathbf{r}}b_{x\mathbf{r}}),
\end{aligned} \tag{2.13}$$

$$C_{\mathbf{r},\mathbf{r}'} = \begin{cases} e^{\pm i2\pi n\phi}, & (\mathbf{r})_x=(\mathbf{r}')_x=na;\\ 1, & (\mathbf{r})_x\neq(\mathbf{r}')_x. \end{cases}$$

This Hamiltonian incorporates the first non-vanishing effects of rotation and can be used as an effective Hamiltonian if $(t_{\parallel}+t_{\perp})/\hbar\Omega$ is not large. However, to investigate corrections for slower rotation one has to go to higher orders as in Eq. (2.11). In Eq. (2.13), we display the vector potential $\mathbf{A}$ explicitly to express the gauge invariance of the effective Hamiltonian. Note that the phase factor in which $\mathbf{A}$ appears is the usual Peierls phase factor which modifies the hopping of particles in the lowest band [see Eq. (1.27)].

For bosons, the short-range repulsive interactions between particles can be incorporated into our model as an on-site interaction energy which can be written, up to terms renormalizing the chemical potential (terms linear in $n_{\mathbf{r}}$), as [58]

$$\begin{aligned}
H_{int} &= \frac{U}{2}\sum_{\mathbf{r}}\left(n^2_{\mathbf{r}}-\frac{L^2_{z\mathbf{r}}}{3\hbar^2}\right),
\end{aligned} \tag{2.14}$$

$$U = g\int|w_{p_{x,y}}(\mathbf{r})|^4 d\mathbf{r},$$

where $n_{\mathbf{r}} = \sum_\mu b^\dagger_{\mu\mathbf{r}} b_{\mu\mathbf{r}}$ is the boson number operator, $L_{z\mathbf{r}} = -i\hbar(b^\dagger_{x\mathbf{r}} b_{y\mathbf{r}} - b^\dagger_{y\mathbf{r}} b_{x\mathbf{r}})$ is the z component of the angular momentum of a boson at site $\mathbf{r}$, and $g > 0$ is the short-range repulsive interaction strength. The interaction Hamiltonian can be written in a microscopically more revealing way using $n^\pm_{\mathbf{r}} = (b^\pm_{\mathbf{r}})^\dagger b^\pm_{\mathbf{r}}$. In this notation $n_{\mathbf{r}} = n^+_{\mathbf{r}} + n^-_{\mathbf{r}}$ and $L_{z\mathbf{r}} = -\hbar(n^+_{\mathbf{r}} - n^-_{\mathbf{r}})$. So the interaction becomes

$$H_{int} = \frac{2U}{3} \sum_{\mathbf{r}} [(n^+_{\mathbf{r}})^2 + (n^-_{\mathbf{r}})^2 + 4 n^+_{\mathbf{r}} n^-_{\mathbf{r}}]. \tag{2.15}$$

By adding H_{int} [Eq. (2.15)] to H_{eff} [Eq. (2.11) or (2.13)], we obtain the Hamiltonian for interacting bosons in the p band of a rotating optical lattice.

Let us end the chapter with a summary of our findings about the p band. By specifically focusing on the first excited band of a two dimensional lattice, we considered how the degenerate excited bands of a tight-binding optical lattice are affected by the effective magnetic field created by rotation. We pointed out that the magnetic field causes not only the hopping between different lattice sites to be modified, but also changes the on-site energies. We showed that once the modification of the on-site energies is explicitly taken into account, the Peierls substitution scheme can be used to obtain an effective Hamiltonian and the energy spectrum of the system. The spectrum contains not only the splitting of the two bands under the effective magnetic field, but also the fine structure forming a pattern similar to the Hofstadter butterfly. We compared the energies obtained from the Peierls substitution procedure with a direct numerical solution of the Schrödinger equation, and observed that our procedure matches the numerical solution to a very good accuracy. By investigating how operator transformations are modified through Peierls substitution [Eq. (2.12)] we derived a first order effective Hamiltonian in real space [Eq. (2.13)]. Going to the next order, we obtain a more accurate, but more complicated effective Hamiltonian, which displays how higher order hopping is modified by the effective magnetic field. Finally, we also gave the expression for on-site interactions between bosons in terms of the angular momentum ‘up’ and ‘down’ operators [Eq. (2.15)].

Chapter 3

Bose-Hubbard Model under Rotation

In this chapter, we consider the Bose-Hubbard model in a two dimensional rotating optical lattice and investigate the consequences of the effective magnetic field created by rotation. In the first part, using a Gutzwiller type variational wave function, we find an analytical expression for the Superfluid (SF)–Mott insulator (MI) transition boundary in terms of the maximum eigenvalue of the Hofstadter butterfly. The dependence of the phase boundary on the effective magnetic field turns out to be complex, reflecting the self-similar properties of the single-particle energy spectrum. In the second part, we perform variational Monte Carlo calculations to show that bosons in a rotating optical lattice will form analogs of fractional quantum Hall (FQH) states when the tunneling is sufficiently weak compared to the interactions and the deviation of density from an integer is commensurate with the effective magnetic field. We compare the energies of superfluid and correlated states to one-another and to the energies found in exact diagonalization calculations for small systems. We look at overlaps between our variational states and the exact ground state, characterizing the ways in which FQH correlations manifest themselves near the MI state. We also explore the experimental signatures of these states. This chapter is based on the material of Refs. [55, 70].

3.1 Phase Boundary between the Superfluid and Mott Insulator States

The modification of the Bose-Hubbard Hamiltonian (1.6) for the rotating system is straightforwardly achieved by changing the hopping term with the Hamiltonian (1.27) of the noninteracting problem, so the Hamiltonian which includes on-site interactions in the presence of an effective magnetic field can be written as

$$H = -t \sum_{\langle i,j \rangle} a_i^\dagger a_j e^{iA_{ij}} + \frac{U}{2} \sum_i n_i(n_i - 1) - \mu \sum_i n_i. \tag{3.1}$$

In fact, changing t to $te^{iA_{ij}}$ or more generally t_{ij} to $t_{ij}e^{i\theta_{ij}}$ for arbitrary lattice geometries is a general prescription to account for the effects of the magnetic field on a single non-degenerate band. As already argued in Sec. 1.2, when the hopping term is dominant ($t/U \gg 1$), one expects the system to be in a SF state, while in the opposite limit of strong interactions ($t/U \ll 1$), the system should go into the MI state. The effect of the magnetic field on the transition boundary has been previously explored using a strong coupling expansion for small magnetic fields by Niemeyer *et al.* [71], and numerically within mean-field theory by Oktel *et al.* [72]. Here we introduce a variational approach to provide an analytical expression for the transition boundary.

We use a site dependent Gutzwiller ansatz to describe the system [10]. For the Bose-Hubbard model without magnetic field, this ansatz (and equivalent mean-field theory [11, 12]) gives an accurate description of the phase diagram (see Fig. 1.1). We introduce the variational wave function at each site l

$$|G_l\rangle = \Delta_l |n_0 - 1\rangle_l + |n_0\rangle_l + \Delta_l' |n_0 + 1\rangle_l. \tag{3.2}$$

Since we investigate the behavior in the vicinity of the transition region, we consider small variations around the perfect MI state with exactly n_0 particles per site, allowing for only one less or one more particle in a site. The variational parameters Δ_l and Δ_l' are assumed to be real, as complex Δ values can only increase the energy of the variational state. Total wave function is the direct product of these site wave functions $|\Psi\rangle = \prod_i^N |G_i\rangle$. As in our previous discussion of the single-particle spectrum, within the Landau gauge, the magnetic Hamiltonian has translational invariance in the y direction. The translational invariance in the x direction is broken by the magnetic field, but can be restored to a certain degree if the flux per plaquette is a rational number. Thus, taking $\phi = p/q$ where p and q are relatively prime integers, the Hamiltonian is invariant under translation by q sites in the x direction. This periodicity simplifies the calculation of the expectation value of the energy when we work with a supercell of $1 \times q$ sites. Total wave function for such a supercell is $|\Psi_s\rangle = \prod_{l=0}^{q-1} |G_l\rangle$. The expected value of the energy can then be written as follows

$$\frac{\langle\Psi|H|\Psi\rangle}{\langle\Psi|\Psi\rangle} = N_s \frac{\langle\Psi_s|H|\Psi_s\rangle}{\langle\Psi_s|\Psi_s\rangle} \equiv N_s \varepsilon, \tag{3.3}$$

where N_s is the number of supercells. To find the expected value of energy for a supercell we will separately calculate the expected values for each term in the Hamiltonian (3.1). In the following calculations we keep terms up to second order in the variational parameters Δ. We start with the chemical potential term

$$\begin{aligned} -\mu\langle\Psi_s|\sum_{l=0}^{q-1} n_l|\Psi_s\rangle &= -\mu\sum_{l=0}^{q-1}\langle G_l|n_l|G_l\rangle\frac{\langle\Psi_s|\Psi_s\rangle}{\langle G_l|G_l\rangle} \\ &\simeq -\mu\sum_{l=0}^{q-1}\Big\{\Delta_l^2(n_0-1)+(\Delta_l')^2(n_0+1) \\ &+ [1-\Delta_l^2-(\Delta_l')^2]n_0\Big\}\langle\Psi_s|\Psi_s\rangle. \end{aligned}$$

In the same manner, we calculate the expected value of the on-site interaction term to be

$$\begin{aligned} \frac{U}{2}\langle\Psi_s|\sum_{l=0}^{q-1} n_l(n_l-1)|\Psi_s\rangle &= \frac{U}{2}\sum_{l=0}^{q-1}\langle G_l|n_l(n_l-1)|G_l\rangle\frac{\langle\Psi_s|\Psi_s\rangle}{\langle G_l|G_l\rangle} \\ &\simeq \frac{U}{2}\sum_{l=0}^{q-1}\Big\{\Delta_l^2(n_0-1)(n_0-2)+(\Delta_l')^2(n_0+1)n_0 \\ &+ [1-\Delta_l^2-(\Delta_l')^2]n_0(n_0-1)\Big\}\langle\Psi_s|\Psi_s\rangle. \end{aligned}$$

As for the hopping term, we introduce a second index for the operators and site wave functions to allow for hopping in the y direction (between supercells). Note that $|G_l\rangle$ actually represents the set of all site wave functions having the same x $(= la)$ coordinate and related to each other by $|G_{lk}\rangle = \exp(i\theta)|G_{lk'}\rangle$, where θ is some possible phase. The expected value of the hopping term (written explicitly for a supercell with $y = ka$) then becomes

$$\begin{aligned}
-t\langle\sum_{\langle i,j\rangle} a_i^\dagger a_j e^{iA_{ij}}\rangle &\to -t\langle\Psi_s|\sum_{\langle l,l'\rangle,k'} a_{lk}^\dagger a_{l'k'} e^{iA_{lk,l'k'}}|\Psi_s\rangle \\
&\simeq -t\sum_{l=0}^{q-1}\Big[(\langle G_{lk}|a_{lk}^\dagger|G_{lk}\rangle\langle G_{l+1,k}|a_{l+1,k}|G_{l+1,k}\rangle + c.c.) \\
&+ \langle G_{lk}|a_{lk}^\dagger|G_{lk}\rangle\langle G_{l,k-1}|a_{l,k-1}|G_{l,k-1}\rangle e^{i2\pi\phi l} \\
&+ \langle G_{lk}|a_{lk}^\dagger|G_{lk}\rangle\langle G_{l,k+1}|a_{l,k+1}|G_{l,k+1}\rangle e^{-i2\pi\phi l}\Big]\langle\Psi_s|\Psi_s\rangle \\
&= -2t\sum_{l=0}^{q-1}\Big[(\Delta_l\sqrt{n_0} + \Delta_l'\sqrt{n_0+1})(\Delta_{l+1}\sqrt{n_0} + \Delta_{l+1}'\sqrt{n_0+1}) \\
&+ \cos(2\pi\phi l)(\Delta_l\sqrt{n_0} + \Delta_l'\sqrt{n_0+1})^2\Big]\langle\Psi_s|\Psi_s\rangle,
\end{aligned}$$

where the last equality is obtained upon the substitution $\langle G_l|a_l|G_l\rangle = \langle G_l|a_l^\dagger|G_l\rangle$ $= \Delta_l\sqrt{n_0} + \Delta_l'\sqrt{n_0+1}$. We did not bother to divide the expression by terms such as $\langle G_l|G_l\rangle\langle G_{l+1}|G_{l+1}\rangle$, since it already contains only second order terms and such a division would have no effect up to second order. Summation of these separate energies yields the energy ε of a supercell defined in Eq. (3.3)

$$\begin{aligned}
\varepsilon = \sum_{l=0}^{q-1}\Big(&-2t\Big\{n_0\Delta_l\Delta_{l+1} + \sqrt{n_0(n_0+1)}\Delta_l\Delta_{l+1}' + \sqrt{n_0(n_0+1)}\Delta_{l+1}\Delta_l' \\
&+ (n_0+1)\Delta_l'\Delta_{l+1}' + \cos(2\pi\phi l)[n_0\Delta_l^2 + 2\sqrt{n_0(n_0+1)}\Delta_l\Delta_l' + (n_0+1)(\Delta_l')^2]\Big\} \\
&+ \frac{U}{2}[2(1-n_0)\Delta_l^2 + 2n_0(\Delta_l')^2 + n_0(n_0-1)] + \mu[\Delta_l^2 - (\Delta_l')^2 - n_0]\Big). \qquad (3.4)
\end{aligned}$$

If the system favors to be in the Mott insulator state, the total energy of the system should be a minimum where all the variational parameters vanish.

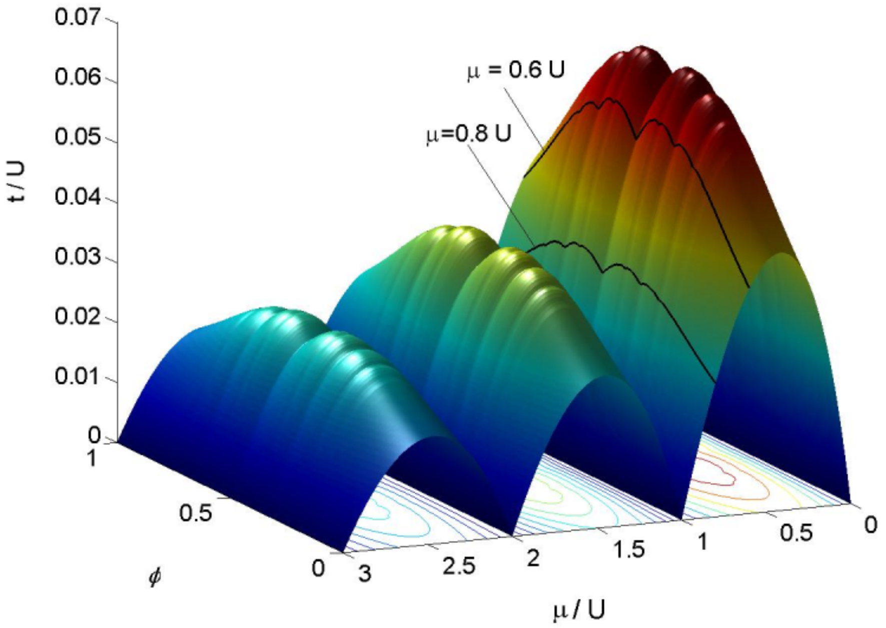

Figure 3.1: The boundary of the Mott insulator phase for the first three Mott lobes. Magnetic field increases the critical value for t/U, as expected, however this increase is not monotonic. There is also a symmetry with respect to $\phi = 1/2$. Transition boundary for two different values of μ/U are marked to display the complex structure of the surface.

Thus, we can find the phase boundary as the point where the total energy ceases to be a local minimum in Δ. As a result, we demand that the matrix composed of the second derivatives of ε with respect to the parameters ($\partial^2\varepsilon/\partial\Delta_i\partial\Delta_j$, $\partial^2\varepsilon/\partial\Delta_i\partial\Delta'_j$, $\partial^2\varepsilon/\partial\Delta'_i\partial\Delta'_j$) be positive definite, i.e. all eigenvalues be positive. This matrix (scaled by U for convenience) can be written compactly as:

$$\begin{aligned}\mathbb{F} &= -\frac{2t}{U}\begin{pmatrix} n_0\mathbb{A}_q & \sqrt{n_0(n_0+1)}\mathbb{A}_q \\ \sqrt{n_0(n_0+1)}\mathbb{A}_q & (n_0+1)\mathbb{A}_q \end{pmatrix} \\ &+ \begin{pmatrix} 2(1-n_0+\mu/U)\mathbb{I}_q & 0 \\ 0 & 2(n_0-\mu/U)\mathbb{I}_q \end{pmatrix},\end{aligned}$$

where $\mathbb{I}_q$ is the $q\times q$ identity matrix, and $\mathbb{A}_q$ was introduced before [Eq. (1.29)] in relation to the single-particle problem.

If we denote the eigenvalues and eigenvectors of $\mathbb{A}_q$ by λ_ν and $\overrightarrow{\nu}$, and those of $\mathbb{F}$ by λ_u and $\overrightarrow{u}$, all λ_u can be expressed in terms of λ_ν by taking

$$\overrightarrow{u} = \begin{pmatrix} a\overrightarrow{\nu} \\ b\overrightarrow{\nu} \end{pmatrix},$$

due to the special block form of $\mathbb{F}$. Then λ_u are obtained as:

$$\begin{aligned}\lambda_u^{\mp} &= 1-(1+2n_0)\frac{t}{U}\lambda_\nu \\ &\mp \sqrt{[(1+2n_0)\frac{t}{U}\lambda_\nu-1]^2-4\{(n_0-\frac{\mu}{U})[1-(n_0-\frac{\mu}{U})]-\frac{t}{U}(1+\frac{\mu}{U})\lambda_\nu\}}.\end{aligned}$$

The positive definiteness of $\mathbb{F}$ leads us to take λ_u^- and set it to 0 in order to determine the critical t/U value above which the perfect insulator state is destroyed. We find the boundary of the n_0th Mott lobe to be:

$$(t/U)_{\text{critical}} = \frac{(n_0-\mu/U)[1-(n_0-\mu/U)]}{f(\phi)(1+\mu/U)}, \tag{3.5}$$

where $n_0-1 \le \mu/U \le n_0$. This boundary is plotted in Fig. 3.1 for the first three Mott lobes. At $\phi=0$, this formula reproduces the critical t/U value found in [11, 12] [see Eq. (1.11)]. Increasing magnetic field increases the critical hopping strength, however this increase is not monotonic. The complicated structure of the single particle problem is reflected in the transition boundary. Equation (3.5) is in excellent agreement with the numerical mean-field work [72].

At zero magnetic field the mean-field result for the transition boundary is close to accurate Monte Carlo calculations [73], but it is not guaranteed that the mean-field description of the system would be valid under magnetic field. Our variational wave function (and mean-field theory) disregards the correlations between fluctuations above the insulating state. Such correlations would be expected to wash out the fine structure of the transition boundary (Fig. 3.1). Nevertheless, one may expect the gross features of the mean-field boundary to survive for the real system. The almost linear increase of the transition point for small magnetic fields, periodicity of the system with respect to ϕ (with period 1), and the central dip near $\phi = 1/2$ should be qualitatively correct. There is however one important way that the fluctuations around the Mott insulating state can become correlated. The Hamiltonian (3.1) supports bosonic FQH states as discussed in a number of recent papers [74, 75, 76]. So far, such FQH states have been assumed to appear only in the region of low density where the number of particles per site is less than one. In the next section, we argue that states similar to bosonic FQH states should be present near the MI boundaries, even at higher densities.

3.2 Fractional Quantum Hall States in the Vicinity of Mott Plateaus

As stated before, most previous studies of analogs of fractional quantum Hall states in optical lattices have focussed on the low density limit, where the average occupation number per site is much fewer than one. In the context of cold atoms, Hafezi *et al.* [29] gave an excellent review of the basic physics of this limit (including symmetry and topology arguments), and argued that one can continuously deform a Mott insulating state into a fractional quantum Hall state by varying the strength of an additional superlattice potential [74]. They also proposed using Bragg spectroscopy to probe these states. Palmer *et al.* [76, 77] performed a number of calculations focussed on the role of the trap, detection schemes, and on inhomogeneities which can spontaneously appear in these systems. Bhat, *et al.* [75, 78, 79] carried out full configuration-interaction calculations for a small number of particles in a rotating lattice with hard-wall boundary conditions. Cooper *et al.* analyzed the relevance of composite fermion wave functions to describing these systems [80]. Cooper recently produced a review of the physics of rotating cold atom clouds including analogs of the quantum Hall effect in lattices [13]. These, and our present study, build on initial works motivated by solid state systems [81, 82, 83, 84, 85, 86, 87, 88].

Translating these arguments to higher densities is not completely trivial. In the standard picture, when the density is tuned away from commensurability (meaning that the number of particles per lattice site is not an integer), the system never goes into the MI state, but will always have a superfluid density. If the system is rotating, one further expects that the collective motion of this superfluid will produce a vortex lattice. When the rotation rate is high enough that the number of vortices is comparable to the number of excess particles, it is plausible to argue that the superfluid will be unstable to forming a correlated state of matter with particles bound to vortices–a situation analogous to that found in the FQH effect. In fact, in the following discussion, we will claim that when the deviation of the particle density from an integer value is commensurate with the magnetic flux one can see analogs of the FQH states coexisting with a frozen MI background.

Before presenting our results based on detailed calculations, it will be useful to briefly sketch the ideas leading to our conjecture about the occurrence of FQH states. Let us assume that the particle density is equal to $\langle n \rangle = n_0 + \epsilon$, where n_0 is an integer and $\epsilon << 1$ is the decimal part of the density. With such incommensurate particle number, the system will never be a perfect MI and the chemical potential for this state, plotted on the $\mu - t$ plane, will trace the outline of the Mott lobe as the interaction is increased (Fig. 3.2). However, if the same system is under a magnetic field that is commensurate with the excess particle density, there appears another possibility. Specifically if $\epsilon = \phi/2$ (two

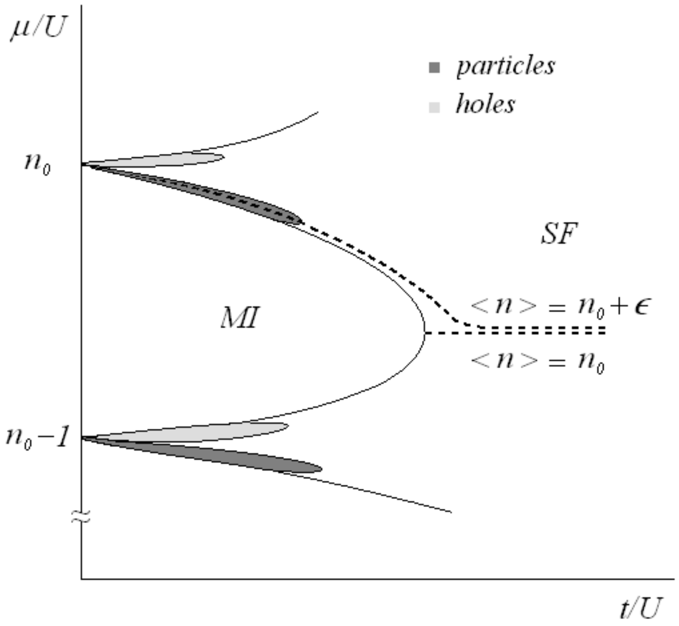

Figure 3.2: Schematic phase diagram near the n_0th Mott lobe. Dotted lines show the chemical potential as a function of hopping strength for systems with constant density $\langle n\rangle = n_0$ and $\langle n\rangle = n_0 + \epsilon$. FQH phases of "excess" particles, or holes are shown as the shaded regions.

flux quanta for one particle), it is possible for n_0 particles to form a MI state that is coexisting with a $\nu = 1/2$ bosonic Laughlin state of the remaining ϵ particles. At high enough interaction, such a state would be preferable to a superfluid state as it avoids any interaction between the "excess" particles.

A variational wave function for such a state can be constructed by symmetrizing the product of the Mott insulator state for n_0 bosons with the $\nu = 1/2$ bosonic Laughlin state for ϵ particles. A crude estimate for the energy of this state can be given in terms of its difference from that of the MI state as

$$\Delta E = [Un_0 - t(n_0 + 1)f(\phi)]\epsilon. \tag{3.6}$$

The first term in brackets is due to the on-site interaction of an excess particle with the MI background and the second term is the hopping energy of the particle in the Hofstadter ground state denoted by $-tf(\phi)$, $f(\phi) > 0$ being the dimensionless maximum eigenvalue of the Hofstadter spectrum. Note that

t is enhanced by a factor of $(n_0 + 1)$ to account for the presence of the Mott background. Interaction effects between excess particles are excluded, as it is expected that in this regime the excess particles avoid one-another. When it is favorable to put one extra particle on to the Mott state, it would be favorable to put more particles (up to ϵ per site) and organize them into a FQH state. One can then expect the correlated state to exist within a band above the MI lobe (see Fig. 3.2). The same argument can be advanced for holes, creating a FQH state of holes below the MI. Experimentally these states would have distinct signatures appearing as extra steps in the density profile near the MI steps of the wedding-cake structure of the trapped system.

Hereafter we confirm this scenario through more rigorous calculations. By using Monte Carlo techniques we compare the energy of variational states describing FQH states and superfluid vortex lattices with each other. We also compare these energies with exact results calculated for small numbers of particles. We find that there is a range of parameters for which the FQH states are more favorable than superfluid states. We note, however, that the energy differences between these states scales as the tunelling energy, and can be quite small.

We start our analysis by writing the Bose-Hubbard Hamiltonian in an effective magnetic field (3.1) with the chemical potential term omitted for now, as we will first work with a definite number of particles

$$H_0 = -t \sum_{\langle i,j \rangle} a_i^\dagger a_j e^{iA_{ij}} + \frac{U}{2} \sum_i n_i (n_i - 1). \tag{3.7}$$

We will also use the gauge $\mathbf{A} = -By\hat{\mathbf{x}}$ for convenience, so the phases $A_{ij} = \exp(ie \int_{\mathbf{r}_j}^{\mathbf{r}_i} \mathbf{A} \cdot d\mathbf{l}/\hbar)$ acquired when hopping in ± x direction are $\mp 2\pi\phi i_y$, where i_y is the y coordinate scaled by lattice constant a, and in y direction $A_{ij} = 0$.

3.2.1 Variational Wave Function

3.2.1.1 Laughlin State

We consider the variational ansatz

$$|\Psi\rangle = \sum_{z_1,...,z_N} \psi(z_1, ..., z_N) a^\dagger_{z_1}...a^\dagger_{z_N}|\Psi_{MI}\rangle, \tag{3.8}$$

where $|\Psi_{MI}\rangle = \prod_j (a^\dagger_j)^{n_0}/\sqrt{n_0!}|0\rangle$ is the Mott insulator state with n_0 particles per site and ψ is the Laughlin wave function [89] with filling $\nu = 1/m$. To describe bosons for which the many-body wave function should be symmetric with respect to a change in the particle coordinates, m must be even. The complex coordinate $z_i = x_i + iy_i$ specifies the location of the ith particle, with i running from 1 to N, where N is the number of excess particles. The sum over z_i is a sum over all lattice sites. To describe a state with excess holes, we replace $a^\dagger$ with a.

To minimize the role of boundaries, the model in (3.7) is typically either solved on a sphere or a torus. We will work in an $L \times L$ torus geometry, corresponding to quasiperiodic (twisted) boundary conditions

$$\begin{aligned} \psi(..., z_k + L, ...) &= \psi(..., z_k, ...) \\ \psi(..., z_k + iL, ...) &= e^{-i\frac{2\pi m N}{L}x_k}\psi(..., z_k, ...), \end{aligned} \tag{3.9}$$

For these boundary conditions the Laughlin wave function can explicitly be written as [90]

$$\begin{aligned} \psi(z_1, ..., z_N) = {} & \mathcal{N} e^{iK_x \sum_i x_i} e^{-K_y \sum_i y_i} e^{-\frac{\pi m N}{L^2}\sum_i y_i^2} \\ & \times \prod_{\beta=1}^{m} \vartheta_1[(Z - Z_\beta)\frac{\pi}{L}] \prod_{i<j}^{N} \left\{\vartheta_1[(z_i - z_j)\frac{\pi}{L}]\right\}^m . \end{aligned} \tag{3.10}$$

Here, $\mathcal{N}$ is the normalization factor, $Z = \sum_i z_i$ is N times the center-of-mass coordinate, $Z_\beta = X_\beta + iY_\beta$ are the *a priori* arbitrary locations of the center-of-mass zeros. To satisfy the boundary conditions, one requires $\sum_\beta X_\beta = n_1 L$

($n_1 \in \mathbb{Z}$), $K_x = 2\pi n_2/L$ ($n_2 \in \mathbb{Z}$), and $K_y = -2\pi \sum_\beta Y_\beta/L^2$. The quasi-periodic Jacobi theta functions are defined by

$$\vartheta_1(z, e^{i\pi\tau}) = \sum_{-\infty}^{\infty} (-1)^{n-1/2} e^{i\pi\tau(n+1/2)^2} e^{(2n+1)iz}.$$

For our square geometry $\tau = i$. This function is odd with respect to z and has the following quasi-periodicity properties: $\vartheta_1(z+\pi) = -\vartheta_1(z)$ and $\vartheta_1(z+\tau\pi) = -e^{-i\pi\tau}e^{-2iz}\vartheta_1(z)$. The relation between the flux quantum per plaquette $\phi = N_\phi/L^2$, filling fraction $\nu = N/N_\phi$, and excess particle density $\epsilon = N/L^2$ is succinctly given by $\phi\nu = \epsilon$, where N_ϕ denotes the number of flux quanta in the $L \times L$ lattice we consider. In what follows, we will restrict ourselves to the $\nu = 1/2$ Laughlin state ($m = 2$), so that the commensurability requirement between the magnetic flux and particle density becomes $\phi = 2\epsilon$.

3.2.1.2 Superfluid State

We will compare the Laughlin state introduced in Sec. 3.2.1.1 with a Gutzwiller mean field state

$$|\Psi_{MF}\rangle = \prod_i \left(\sum_n f_n^i |n\rangle_i \right), \tag{3.11}$$

where f_n^i are variational parameters. In the non-rotating case, the superfluid is translationally invariant, and the coefficients f_n^i are independent of i [see Eq. (1.9)]. In our case, where the lattice is rotating, a vortex lattice forms, breaking translational invariance.

Near the Mott lobe, the site occupations are dominated by $n = n_0$ and $n = n_0 \pm 1$, i.e. it is extremely unlikely to have more than one extra particle or hole at a given site [see Eq. (3.2)]. We therefore truncate our basis to only these three values of n. This will also facilitate direct comparison with exact diagonalization calculations using the same truncated basis. We work in an $L \times L$ lattice, using the boundary conditions which are equivalent to those in Eq. (3.9).

The numerical technique for optimizing the parameters f_n^i [see the discussion following Eq. (1.9)] can be described in terms of a variational calculation where one minimizes $\langle\Psi_{MF}|H_0|\Psi_{MF}\rangle$ with the constraints that the total number of particles M and normalization $\langle\Psi_{MF}|\Psi_{MF}\rangle$ are fixed: this involves introducing the chemical potential μ as a Lagrange multiplier. In practice it is more convenient to write $H = H_0 - \mu M$, and follow an iterative procedure based upon mean field theory. These two approaches are completely equivalent. In comparing energies with our other variational state, one must be cautious and be sure to use $\langle H_0\rangle = \langle H\rangle + \mu M$.

3.2.2 Exact Results on Small Systems

For small systems we can exactly diagonalize the Hamiltonian in Eq. (3.7), taking a configuration-interaction approach where we truncate the allowed number of particles on a given site to be n_0, $n_0 - 1$, or $n_0 + 1$. For definiteness we take $n_0 = 1$: changing this value just scales the hopping matrix elements t. For these small system sizes we can also directly calculate $\langle\Psi|H_0|\Psi\rangle$. In Sec. 3.2.3 we will discuss larger systems where we need to resort to a Monte Carlo algorithm for calculating this energy.

We consider 12 particles in a 3×3 lattice, so that the excess particle density is 1/3. We take $\nu = 1/2$ and accordingly the number of quanta of flux per plaquette is $\phi = 2/3$. Fig. 3.3 displays the energies (measured in units of U) of the first few hundred exact energy eigenstates together with the energies of our two variational wave functions: Eqs. (3.8) and (3.11). We emphasize that our ansatz for the fractional quantum Hall state is not just the Laughlin state, where flux is bound to each particle, but is rather the coexistence of a Mott state and a Laughlin state, with flux bound only to the excess particles. In Fig. 3.3 we also show the estimated energy from Eq. (3.6). It is remarkable how closely this estimate matches the results of the exact diagonalization for small t.

For $t \lesssim 0.13$ the energy of our candidate fractional quantum Hall state

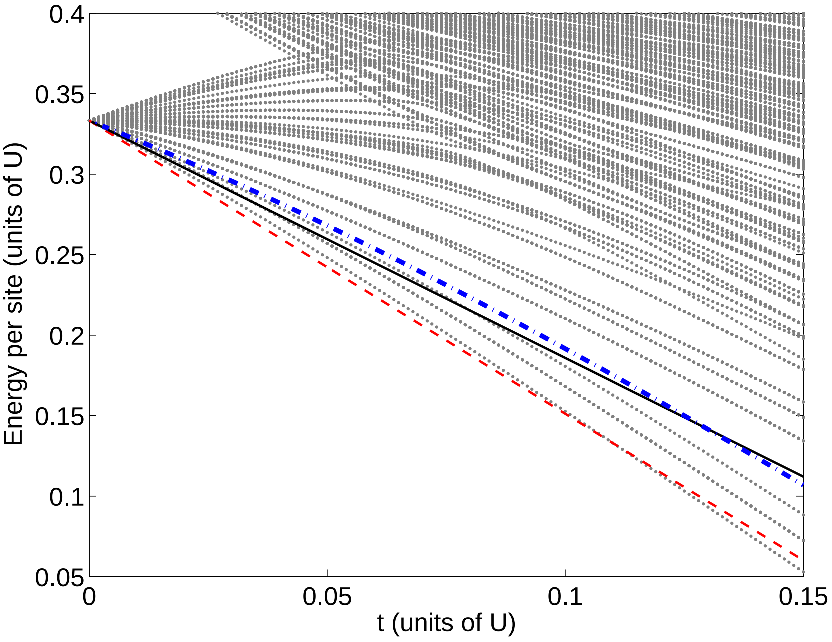

Figure 3.3: Exact many-body spectrum for 12 particles in a 3×3 lattice with $\phi = 2/3$ considering only 0,1, and 2 atoms per site (for $\nu = 1/2$, excess particle density is $\epsilon = \phi\nu = 1/3$). Also shown by the solid black line is our variational estimate of the energy of a fractional quantum Hall state of excess particles in the presence of a Mott background. Dash-dotted blue line shows the Gutzwiller mean-field superfluid energy for the same density $(1+\epsilon)$, corresponding to a vortex lattice where the cores are filled with Mott insulator. The dashed red line is the estimate of the ground state energy from Eq. (3.6), first introduced in [55]. For low enough t the variational energy of the correlated state of excess particles is lower than the superfluid energy.

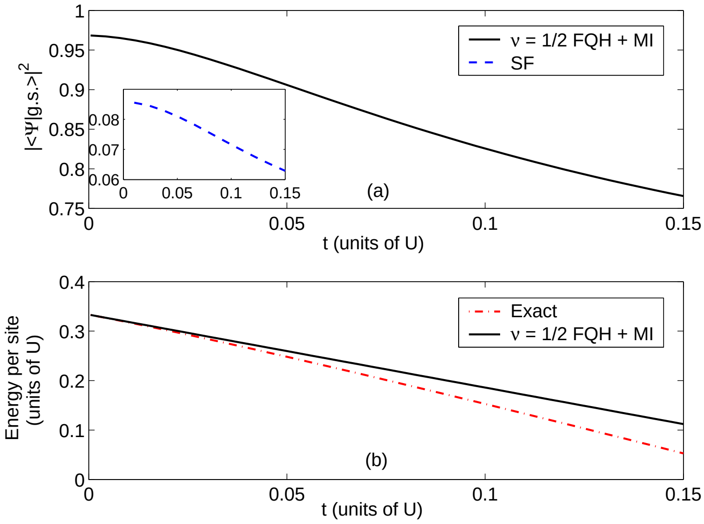

Figure 3.4: (a) Overlap between the $\nu = 1/2$ FQH + MI state [$|\Psi\rangle$ from Eq. (3.8)] and the exact ground state [$|\text{g.s.}\rangle$, determined from diagonalizing Eq. (3.7) in a truncated basis] as a function of tunneling strength t, using the same parameters as Fig. 3.3. Also shown in the inset is the overlap between a superfluid vortex lattice and $|\text{g.s.}\rangle$. (b) Comparison of the variational and exact energies – from Fig. 3.3.

(with optimized Z_β) is lower than that of the superfluid, while the opposite holds for larger t. Our physical picture of this is that as t grows the Mott insulator melts, and the density of mobile atoms is no longer commensurate with the magnetic field. For very small t, the variational energy agrees very well with the exact ground state energy, which is shown more clearly in Fig. 3.4(b). In Fig. 3.4(a) we show the overlap between our variational state and the exact ground state. At low t the overlap is greater than 95%, but it falls off with increasing t presumably due to the increasing importance of particle-hole excitations. The overlap between the ground state and the mean-field superfluid [inset of Fig. 3.4(a)] is never large, and their energies in Fig. 3.3 never approach one-another. We believe this is due in part to the fact that the mean-field state breaks translational invariance, and consequently involves a superposition of many eigenstates [91]. A quantum superposition of vortex lattices, may in fact be a good alternative description of the FQH state.

Given the small difference between the energies of our two variational states,

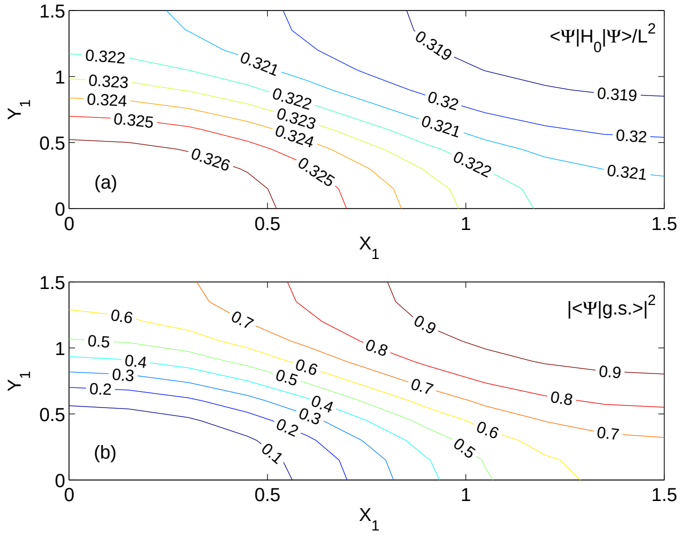

Figure 3.5: Variational energy (in units of U) (a) and the overlap with the exact ground state (b) as a function of center of mass zeros $Z_1 = X_1 + iY_1$, $Z_2 = L - Z_1$, measured in units of the lattice constant. As with Fig. 3.3, we consider an $L \times L$ cell with $L = 3$, flux per plaquette $\phi = 2/3$, filling factor $\nu = 1/2$ and total particle number $M = 12$. We take $K_x = 0$, $K_y = 0$, and $t = 0.01U$. The lower the variational energy, the higher the overlap. The lowest energy occurs for $X_1 = Y_1 = L/2$ where the overlap is 96.4%. At this point, the variational energy is $0.3186U$, which is very close to the exact ground state energy of $0.3176U$.

one must be somewhat cautious about ascribing too much significance to the crossing at $t \sim 0.13$. One also might be concerned that at that value of t, both variational states have an energy which is significantly higher than that of the ground state, suggesting that neither may be particularly good descriptions of the true ground state. A third concern is that there is no sign of a phase transition in Fig. 3.4(a): the overlap between the fractional quantum Hall state and the exact ground state remains above 75% out to $t \sim 0.15$. Despite these caveats, the large overlaps at small t is convincing evidence that the ground state at low t is a fractional quantum Hall state of excess particles.

In Fig. 3.5 we show how the energy of the variational state depends on the parameters Z_β, which represent where "vortices" can be found around which the center of mass flows. The boundary conditions in Eq. (3.9) force the wave function to have $m = 1/\nu$ of these zeros (in the present case $m = 2$). In the absence of the lattice, the energy is invariant under changing these parameters, leading to an m-fold degeneracy of the ground state [92]. Here this symmetry is absent and the energy depends on Z_β. Not surprisingly, the overlap between the variational state and the exact ground-state is directly correlated with the energy. This overlap has a maximum when the variational energy has a minimum.

3.2.3 Variational Monte Carlo Method

Unfortunately the maximum size of the system which can be treated by the techniques of Sec. 3.2.2 is quite limited. Our preceding results for small system size predominantly serve as a guide for physical intuition, and cannot quantitatively describe the physics of the infinite system. Here we introduce a variational Monte Carlo (VMC) algorithm [93, 94, 95, 96] in order to calculate the energy $\langle\Psi|H|\Psi\rangle = \langle\Psi|H_0 - \mu M|\Psi\rangle$, where M is the total number of particles. This will allow us to make a more solid comparison of the energies of the superfluid and correlated states, and draw the phase diagram in Fig. 3.6. This phase diagram illustrates the regions of $\mu - t$ plane where either the superfluid or correlated state has a lower energy.

We begin by introducing a basis $|R = \{z_1, \cdots, z_N\}\rangle$ where the N excess particles are at sites z_1 through z_N. This allows us to write

$$\begin{aligned}
\langle\Psi|H|\Psi\rangle &= \sum_{RR'}\langle\Psi|R\rangle\langle R|H|R'\rangle\langle R'|\Psi\rangle = \sum_R P_R E_R, \\
P_R &= |\langle R|\Psi\rangle|^2, \qquad (3.12)\\
E_R &= \sum_{R'}\frac{\langle R|H|R'\rangle\langle R'|\Psi\rangle}{\langle R|\Psi\rangle}.
\end{aligned}$$

We use a Metropolis algorithm to sample the sum over R. Starting from some configuration R_0 we generate a new one R_1 by attempting to move a single particle by one site. We accept the move with probability $\min\{1, \mathrm{P_{R_1}/P_{R_0}}\}$: we then continue the procedure to generate R_2, R_3, ... In the resulting

Markov chain each configuration R will appear with probability P_R. After S steps, the energy is then estimated as $E_S = \sum_{i=1}^{S} E_{R_i}/S$. As is usual, we discard the first few thousand steps so as not to bias the sum by our choice of initial configuration. We use a binning analysis to estimate the statistical error on our sum [97].

Since the Hamiltonian connects only a finite number of different configurations (those which differ by moving one particle by one site), the sum is numerically straightforward and we calculate E_R for each R directly. As a further simplification we note that $E(\mu, t) = E_0(\mu) - (n_0 + 1)tK$, where $E_0 = Un_0\epsilon + U(n_0 - 1)n_0/2 - \mu(n_0 + \epsilon)$ is the expectation value of the on-site terms in H and $-(n_0 + 1)tK$ is the expectation value of the hopping energy. K is independent of n_0, as the only role of the Mott background is to provide a Bose-enhancement term of $(n_0 + 1)$. By using the Monte Carlo algorithm to calculate K, rather than E, we produce $E(\mu, t)$ for all n_0, μ, and t at once.

Table 3.1 lists the parameters for which we have performed VMC calculations. For the smallest system sizes ($L = 3, 4, 5$) we find that the VMC agrees with the direct calculation of the variational energy. From the chart, we conclude that finite size effects are significant in the $L = 3$ cases, but for larger L the differences between the energies of the two systems are within a few percent.

Fig. 3.6 illustrates our results for $\phi = 1/4$. Near the constant density line $\langle n \rangle = 1 + \epsilon$, there is a region where our variational wave function has a lower energy than the Gutzwiller mean field vortex lattice. This corresponds to an incompressible $\nu = 1/2$ bosonic Laughlin state above the $n_0 = 1$ Mott insulator. The same argument can be advanced for holes by just changing the creation operators in Eq. (3.8) with annihilation operators leading to a coexisting Mott insulator and FQH state of holes near the $\langle n \rangle = 1 - \epsilon$ line, although it is less visible than in the particle case.

One of the promising schemes for observing the incompressible states described here is through *in situ* imaging of the density profile of a trapped gas

ϕ	ϵ	L	N	K	δK
2/3	1/3	3	3	0.7376	6×10^{-4}
		6	12	0.5187	4×10^{-4}
4/9	2/9	3	2	0.4419	4×10^{-4}
		6	8	0.4455	2×10^{-4}
8/25	4/25	5	4	0.3874	1×10^{-4}
		10	16	0.3873	5×10^{-5}
1/4	1/8	4	2	0.3483	2×10^{-4}
		8	8	0.3375	4×10^{-5}

Table 3.1: Results of our variational Monte Carlo calculation. ϕ is the number of flux per plaquette, ϵ is the density of excess particles, L is the system size, N is the number of excess particles, $-(1+n_0)tK$ is the hopping energy per site, where t is the hopping matrix element and n_0 is the number of particles per site in the underlying Mott state. K is dimensionless. Our estimates of the statistical error in K from a binning analysis of 80 000 samples are given by δK.

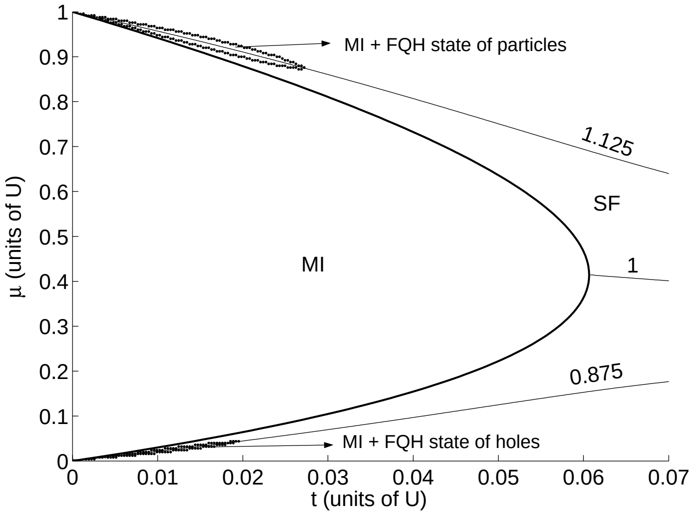

Figure 3.6: Phase diagram for $\phi = 1/4$ and $\nu = 1/2$. Boundary between Mott insulator (MI) and superfluid (SF) states is found from a mean-field calculation. Excess particle (or hole) density is $\epsilon = \phi\nu = 0.125$. Boundary of the coexistent $\nu = 1/2$ FQH state of excess particles (holes) and $n_0 = 1$ MI state centered around the 1.125 (0.875) constant density line is determined from a comparison of VMC and mean-field energies. We consider 8 particles in an 8×8 lattice in the VMC calculation.

[76, 77, 98]. The FQH states should appear as extra steps in the density profile near the Mott insulator plateaus. Moreover, the behavior of these steps is predictable: the density is set by the magnetic flux, and the size of the gap (hence the spatial size of the plateau) increases with magnetic field. One can even imagine that for a fixed flux there will appear a sequence of FQH states with larger even denominators and thus with smaller densities all the way up to the SF–MI phase boundary, however their size will be much smaller and they may not be discernible at all. Other probes for the FQH states may be noise correlations in time-of-flight experiments, measurement of the Hall conductance for the mass current in a tilted lattice, or Bragg spectroscopy [74, 75, 76, 78, 79, 29, 77, 13, 98, 80]. A major obstacle to the observation of these states is the need to reduce the temperature to below the scale of the gap, which is a fraction of the hopping strength t. Such temperatures are currently hard to reach reliably.

In summary, we have predicted that experiments on bosons in lattices with an effective magnetic field will see a phase where the excitations on top of a Mott insulator form a bosonic fractional quantum Hall state. We base our prediction on a set of variational calculations, supplemented by exact diagonalization of small systems. We find that the MI + $\nu = 1/2$ Laughlin state has a lower energy than the mean-field vortex lattice when the density of excess particles or holes, $\epsilon = N/L^2$, is chosen appropriately ($\epsilon = \phi\nu = \phi/2$), and the hopping t is sufficiently small compared to the interactions U. In this regime we find that the overlap between the exact ground state and the proposed coexistent state is as large as 96%, but the overlap with the superfluid is smaller than 10%. We produced a phase diagram (Fig. 3.6), illustrating where this novel phase should be found at low temperatures.

Chapter 4

Realization of the Hofstadter Insulator

In this chapter, we consider a gas of noninteracting spinless fermions in a rotating optical lattice and calculate the density profile of the gas in an external confinement potential. The density profile exhibits distinct plateaus, which correspond to gaps in the single-particle Hofstadter spectrum. These plateaus result from insulating behavior whenever the Fermi energy lies within a gap. We discuss the necessary conditions to realize this Hofstadter insulator in a cold-atom setup and show how the quantized Hall conductance can be measured from density profiles. The discussion is based on the material of Ref. [98].

The gaps in the Hofstadter spectrum form continuous regions for a finite range of flux. For a system of noninteracting fermions, it was shown by Thouless *et al.* that whenever the Fermi energy lies in one of these gaps, the Hall conductance of the system is quantized [81]. This quantization is topological in nature, and the quantized Hall conductance is determined uniquely by the magnetic translation symmetry [51]. This Hofstadter insulating phase is a topological insulator that can be characterized by two topological numbers [99], the first Chern number corresponding to Hall conductance and another number related to polarizability [100].

As the conventional solid state setups are not suitable for the observation of this spectrum because of the high magnetic field strengths required (see the discussion in Sec. 1.4), we propose an alternative way to achieve and to experimentally study this topological insulator by using ultracold Fermi gases in a rotating optical lattice.

We first discuss the conditions for simulating the Hofstadter model in an ultracold optical lattice system:

(1) Hofstadter model is expressly single band; the motion of fermions in the periodic potential has to be well described by a single-band tight-binding model with nearest neighbor hopping. This requirement means that there has to be a finite gap between s and p bands, and the dispersion of the s band can be well approximated by a cosine function. From the band structure calculations for optical lattice potentials, one can easily show that this requirement is fulfilled when $V_0 > 3E_R$ [101, 102, 103]. A rotating lattice experiment has recently been carried out [27]. Although in this particular experiment $V_0 < 1E_R$, which is not deep enough to reach the tight-binding regime, there is no fundamental reason against increasing V_0 a few more E_R, as it has been routinely done in static lattice experiments [4].

(2) The “magnetic field” has to be strong enough. As we have shown before the magnetic flux quantum per plaquette ϕ is related to the rotation frequency Ω as $\phi = 2ma^2\Omega/h$. For rotation to create an effective magnetic flux close to one flux quantum, the rotation frequency Ω must be close to $E_R/\hbar$ (more rigorously $\phi = \pi\hbar\Omega/2E_R$). In typical optical lattice experiments the recoil frequency is a few kHz, thus, rotation of the lattice at hundreds to thousands of Hz would be enough to reach the high magnetic field limit.

(3) To observe the insulating behavior, the temperature has to be lower than the gap of the insulator. The gap for the Hofstadter insulator is comparable to the hopping amplitude t. In a moderately deep lattice, for which $V_0 \sim 3-7E_R$, for instance, t is of the order of $1-10$ nK. This is below currently attainable

temperatures. However, cooling fermions to this regime is not more difficult than achieving degenerate Fermi gases in a lattice, and the latter is now the major goal pursued in many key laboratories in this field.

(4) The Hofstadter model is a noninteracting one. Strong repulsive or attractive interactions can lead to either exciton instability or BCS instability of the insulating phase (which will be discussed in Ch. 5), and therefore diminish its topological behavior. In ultracold atom experiments a single species of fermions is naturally noninteracting due to the Pauli exclusion principle.

Even when the above conditions are satisfied, there are two factors which complicate the correspondence between the results of ultracold atom experiments and theories developed for 'bulk' systems. The first is the presence of an external confining potential in all ultracold atom experiments, i.e. the third term in Eq. (1.14). The second factor is that transport measurements are usually very hard for cold atom systems. Hereafter, we first calculate the density profile of a noninteracting Fermi gas in a rotating optical lattice, in the presence of a smooth external potential [104]. We find that the presence of the residual trapping potential facilitates the observation of the effects of single-particle spectrum, as long as it is varying smooth enough on the lattice length scale. Secondly, we show that one of the most important transport properties, namely the Hall conductance which reflects the topological nature, can be inferred from the measurement of the density profile due to the well-known Středa formula [105].

4.1 Density Profile for Noninteracting Trapped Fermions in a Rotating Lattice

When the residual trapping potential is slowly varying, we can utilize the local-density approximation (LDA) in which we define a local chemical potential $\mu_l(r)$ (or Fermi energy) as

$$\mu_l(r) = \mu - V(r), \tag{4.1}$$

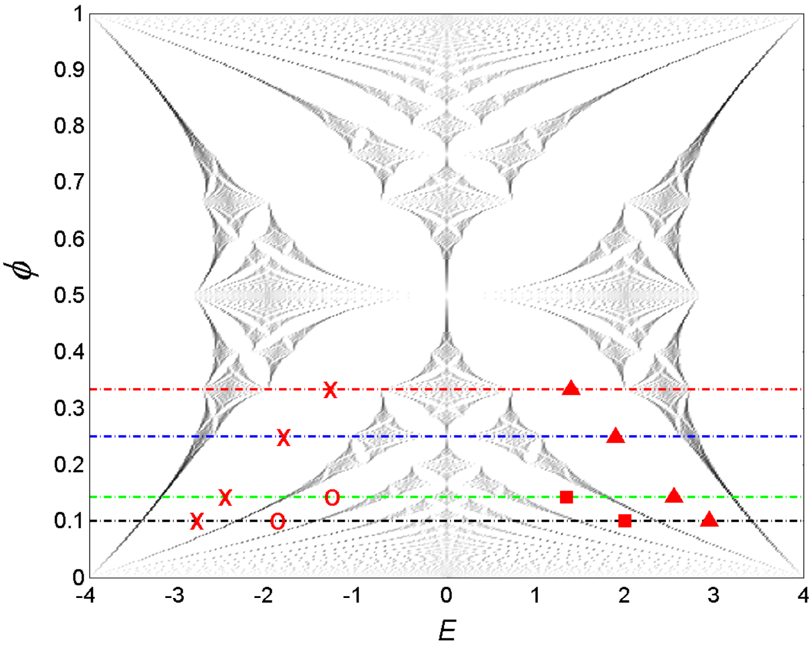

Figure 4.1: Density of states for the Hofstadter butterfly. Darker regions imply greater density. Dashed lines represent the trajectory of local Fermi energy from the center to the edge of the cloud, for different values of ϕ corresponding to those used in Fig. 4.2, namely $\phi = 1/3, 1/4, 1/7$, and $1/10$. Regions marked by $\times$ and $\blacktriangle$ have Hall conductance $\sigma_{xy} = \pm 1$; and marked by $\circ$ and $\blacksquare$ $\sigma_{xy} = \pm 2$.

where in our case $V(r) = m(\omega_\perp^2 - \Omega^2)r^2/2$. In what follows, we shall denote $(\omega_\perp^2 - \Omega^2)$ by ω^2.

To find the density profile $n(r)$, we simply count the number of states below $\mu_l(r)$ for the corresponding uniform system as

$$n(r) = \int d\epsilon D(\epsilon)\Theta(\mu_l(r) - \epsilon). \tag{4.2}$$

The density of states $D(\epsilon)$ is displayed in Fig. 4.1. In the Hofstadter spectrum, for which ϕ is a rational number p/q, the gaps form continuous regions in $\phi - E$ plane, although the band edges are fractal. When μ lies in a gap, the system is an insulator, and as one changes ϕ and μ, the topological nature and the Hall conductance of the insulator do not change as long as one remains within the same gap [81]. The largest two gaps correspond to insulators with Hall conductance $\sigma_{xy} = \pm 1$, and the second largest ones have Hall conductance

$\sigma_{xy} = \pm 2$ and so on, as marked in Fig. 4.1.

To calculate the integral in Eq. (4.2) efficiently, we note that if we take q to be sufficiently large, the bandwidths of each subband become negligibly small. Counting the number of states then reduces to counting these bands in certain intervals. In our numerical procedure, we determine the subbands with their edge values ε_{edge}. So the number of states per plaquette in the two dimensional case can conveniently be expressed as

$$n(\mu) = \frac{1}{2q} \sum_{\varepsilon_{edge}} \Theta(\mu - \varepsilon_{edge}). \tag{4.3}$$

In all of our calculations we took $q = 401$, which is a prime number allowing p to be successive integers. ϕ values for other small denominators of q are approximated by properly choosing p. For instance, $\phi = 1/10$ is approximated by 40/401, 1/4 by 100/401 and 1/3 by 134/401.

We now present the density profiles for several ϕ values. To make a connection with experiments, we refer to the work in Ref. [56] in which the fermionic ^{40}K atoms are stored in an optical lattice with lattice constant $a = 413$ nm. We take $V_0 = 5E_R$, which gives $t = 0.066E_R$. The parameters at hand yield $E_R/\hbar = 45.98$ kHz and $t/\hbar = 3.035$ kHz. With the choice $\omega \sim 355$ Hz, the gas extends over approximately 60 lattice sites in the radial direction, so that the assumption of LDA is satisfied. In Figs. 4.2 and 4.3 we fixed the number of fermions at 5000.

When the local chemical potential $\mu_l(r)$ lies in one of the gaps, we have $\partial n(r)/\partial\mu(r) = 0$ because of vanishing compressibility. Hence, as one can see by comparing Fig. 4.1 and Fig. 4.2, corresponding to the energy gaps in the single particle spectrum, there appear plateaus in the density profile. The discernible number of plateaus is related to the size of the energy gaps. For instance, in Fig. 4.2(a), the plateau with $n = 1$ is the band insulator with completely filled band, which is topologically trivial and has vanishing Hall conductance. Apart from that, for $\phi = 1/3$, the chemical potential trajectory passes through two gap regions which gives two plateaus with $n = 0.333$ and $n = 0.667$ respectively. While for $\phi = 1/4$, there are totally four subbands, but

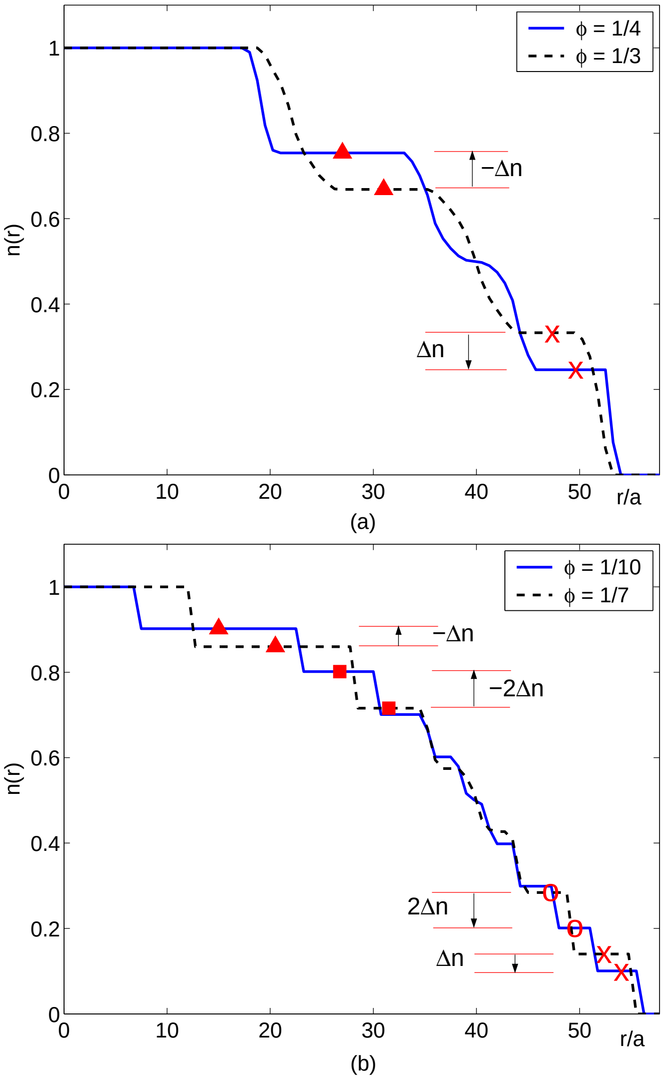

Figure 4.2: (a) Density profiles for 5000 fermions with $\phi = 1/4$, $\Omega = 7.2992$ kHz, $\omega_\perp = 7.3078$ kHz (solid line) and $\phi = 1/3$, $\Omega = 9.7809$ kHz, $\omega_\perp = 9.7873$ kHz (dashed line). (b) Density profiles for 5000 fermions with $\phi = 1/10$, $\Omega = 2.9197$ kHz, $\omega_\perp = 2.9412$ kHz (solid line) and $\phi = 1/7$, $\Omega = 4.1605$ kHz, $\omega_\perp = 4.1756$ kHz (dashed line). Length is measured in units of lattice constant a. Density is given in units of particles per lattice site.

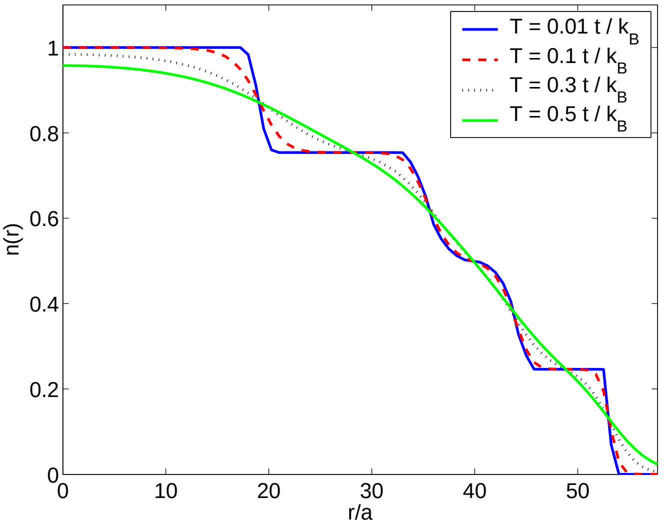

Figure 4.3: Density profile for 5000 fermions at several temperatures when $\phi = 1/4$. Plateaus become indiscernible when $k_BT \sim 0.5t$.

two of them touch at $\mu = 0$, so there are also two gap regions corresponding to two plateaus with $n = 0.25$ and $n = 0.75$. In Fig. 4.2(b) we choose two ϕ's with larger q, where there are more gaps in the spectrum and therefore more density plateaus. Experimentally, the smaller gap one wants to find, the more difficult it is, because it requires much larger system size and much lower temperature.

In Fig. 4.3 we show the temperature effect on the visibility of plateaus. We implement the effect of finite temperature by incorporating the Fermi-Dirac distribution into our calculations as

$$n_{2D}[\mu_l(r), T] = \frac{1}{2q} \sum_{\varepsilon_{edge}} \frac{1}{\exp\{[\varepsilon_{edge} - \mu_l(r)]/k_BT\} + 1}. \tag{4.4}$$

We observe from Fig. 4.3 that plateaus will be smeared out when $k_BT > 0.5t$.

4.2 Quantized Hall Conductance

As shown by Thouless *et al.*, the topological distinction of the insulators we consider manifests itself in the Hall conductance, which should be quantized in units of e^2/h [81]. Here, we propose a method to read out the information about the Hall conductance quantization from the obtained density profiles. With this method one can observe how the particle density within a particular plateau (labelled by the corresponding gap) changes with the rotation frequency. The change of plateau density with respect to rotation frequency is directly related to the Hall conductance of that plateau.

Středa obtained a formula for the Hall conductance of a two dimensional charged system as

$$\sigma_{xy} = e\frac{\partial N}{\partial B}, \tag{4.5}$$

which is valid when the Fermi energy lies in a gap [105]. Here N is the number of levels below the Fermi energy. For a neutral gas we can define a similar response function $\gamma_{xy} = J_x/F_y$, where J_x is the mass current in the x direction induced by a force F_y in the y direction. Then the Středa formula for the rotating system can be rewritten as

$$\gamma_{xy} = \frac{1}{2}\frac{\partial N}{\partial \Omega}. \tag{4.6}$$

Expressing the rotation frequency in terms of ϕ, and N in terms of the density per plaquette $n(r)$ (as in our density plots), one obtains

$$\gamma_{xy} = \frac{m}{h}\frac{\partial n}{\partial \phi}. \tag{4.7}$$

To measure Hall conductance, we first choose two ϕ values, and identify the plateaus in both density profiles that correspond to the same gap. The density difference of those two plateaus divided by the difference between ϕ values gives the Hall conductance. We use Fig. 4.2 as an example to show how this procedure works. The plateaus are marked by the same symbol as their corresponding gaps in Fig. 4.1. Two plateaus marked by the same symbol are the same insulating phase. In Fig. 4.2(a), for that marked by ×, $\Delta n =$

$0.333 - 0.25$, and $\Delta n/\Delta\phi = 1$, for that marked by ▲, $\Delta n = 0.667 - 0.75$, and $\Delta n/\Delta\phi = -1$. In Fig. 4.2(b), one can get the same quantization number for the plateaus marked by × and ▲. In addition, there are more plateaus, such as those marked by ○ and ■ corresponding to the second largest gaps. For that marked by ○, $\Delta n = 0.284 - 0.201$ and $\Delta n/\Delta\phi = 2$, and for that marked by ■, $\Delta n = 0.716 - 0.802$ and $\Delta n/\Delta\phi = -2$.

While the above examples concentrated on the largest, Landau level type, gaps of the spectrum, the method can be applied to any gap, including the nontrivial smaller gaps in the right-left or central chains. For example, considering two density profiles near $\phi = 0.45$ we can observe the Hall conductance of the largest gap in the right chain to be $\Delta n/\Delta\phi = 2$. Generally smaller gaps have higher values of Hall conductance; however, experimentally it becomes increasingly harder to observe these gaps, as the corresponding plateaus will become discernible at lower temperatures and higher particle numbers.

To summarize, we discussed the experimental conditions for simulating the Hofstadter model in rotating optical lattices, such as lattice depth, rotation frequency, and temperature. We calculated the density profile in the presence of a smooth residual trapping potential, and showed how the density plateaus reflect the insulating behavior in a "magnetic field" with incommensurate filling number. We also proposed a method to measure the Hall conductance from real space density profiles, without doing transport experiments.

Chapter 5

Pairing of Fermions in Rotating Lattices

In most conventional metals, for which the magnetic flux quantum per plaquette ϕ is very small ($\phi \ll 1$) the magnetic field can be treated semi-classically as the electron density $n \sim 1$ is several orders larger than ϕ. By contrast, in two-dimensional electron gases, where $n \sim \phi \ll 1$, the density is so low that only the bottom of an electron band is populated, and the effective mass approximation is sufficient to account for the lattice effect. In cold atom systems, however, because the magnetic field is synthetically generated by rotation or by engineering atom-light interactions (see Sec. 1.3), and the lattice spacing is of the order of half a micron, one can access the regime $n \sim \phi \sim 1$, where both the lattice and the magnetic field should be treated on an equal footing and in a quantum-mechanical manner.

For neutral atoms in optical lattices, the interaction is dominated by on-site interactions as we have reviewed the case for bosons in Sec. 1.2. In order to emphasize the inclusion of magnetic field effects in such systems, we will generally refer to the model describing interacting cold atoms in optical lattices with a large magnetic field as the Hofstadter-Hubbard (HH) model. Recently, many works (including ours, see Ch. 3) have focused on the bosonic HH model, which reveal a number of interesting phenomena, including possible fractional quantum Hall states and vortex lattice states [106, 107, 108, 109]. However, so far little attention has been paid to the fermionic HH model (see for instance Ref. [110]). In this chapter, we will investigate the properties of the paired superfluid phase in the fermionic HH model with attractive interactions. Our discussion will be based on the material of Ref. [111].

For $\phi \sim 1$, the pairing problem differs from the usual BCS theory of type-II superconductors in an important way. In type-II superconductors the separation between the vortices is much larger than the size of Cooper pairs, hence one can locally apply the BCS scenario to define a local order parameter $\Delta(\mathbf{r})$, and understand the vortex lattice by coupling this "coarse grained" order parameter to the magnetic field. Because of the second critical field H_{c2} one can never enter the regime where Cooper pair size is smaller than the distance between vortices. In the HH model considered here, magnetic field modifies the single-particle dispersion in a fundamental way and magnetic flux is not negligible even at the shortest length scale, which is the lattice constant. Hence, any discussion of pairing must include the effect of the magnetic field at the microscopic level. We show that such a microscopic theory requires the definition of an order parameter with multiple components. Even though the definition of the order parameter is complicated by the inclusion of the magnetic field at the microscopic level, we see that this order parameter naturally describes the vortex lattice, despite the fact that the separation between the vortices is of the order of lattice spacing.

The main points of our analysis are highlighted as follows.

(1) We first review that for $\phi = p/q$, where p and q are relatively prime integers, each single-particle state in the Hofstadter spectrum is q-fold degenerate due to magnetic translation symmetry. This degeneracy enforces that a comprehensive formulation of BCS theory in this case must contain Cooper pairs with both zero and a set of finite momenta, which are to be treated on an equal footing.

(2) We show that the magnetic translation symmetry also imposes relations

between pairing order parameters of different momentum. These relations are verified numerically by self-consistently solving the BCS mean-field Hamiltonian.

(3) The relative phases between different pairing order parameters determined from self-consistent solutions can also be understood from a more intuitive and simpler Ginzburg-Landau argument.

(4) We determine the structure of vortices in the superfluid ground state using the information from (2). The unit cell of the superfluid phase is enlarged to $q \times q$, whose symmetry is lower than that of the original Hamiltonian. Hence, the superfluid ground state has discrete degeneracy, related to the symmetry of the vortex lattice.

(5) For certain fermion densities, a critical interaction strength is predicted for a quantum phase transition from a Hofstadter insulator to a superfluid phase.

5.1 Generalized BCS Model

We consider a two-component Fermi gas in a two-dimensional optical lattice potential so that an s band tight binding model accurately describes the dynamics. Both components are coupled to the same gauge field $\mathbf{A} = Bx\hat{\mathbf{y}}$, in the Landau gauge. Note that, there is no Zeeman shift associated with a synthetic magnetic field. The single-particle dynamics is described by the Hamiltonian

$$H_0 = -t \sum_{\langle ii' \rangle \sigma} \left(c^{\dagger}_{i\sigma} c_{i'\sigma} e^{iA_{ii'}} + \text{h.c.} \right), \tag{5.1}$$

where $c_{i\sigma}$ ($c^{\dagger}_{i\sigma}$) annihilates (creates) a fermionic particle at site $i = (i_x, i_y)$ with spin σ ($=\uparrow, \downarrow$) and the phases $A_{ii'}$ are again determined for the Landau gauge as in Eq. (1.27). Recall the degeneracy in the k_y direction due to magnetic translation symmetry as expressed in Eq. (1.25), which will be very important

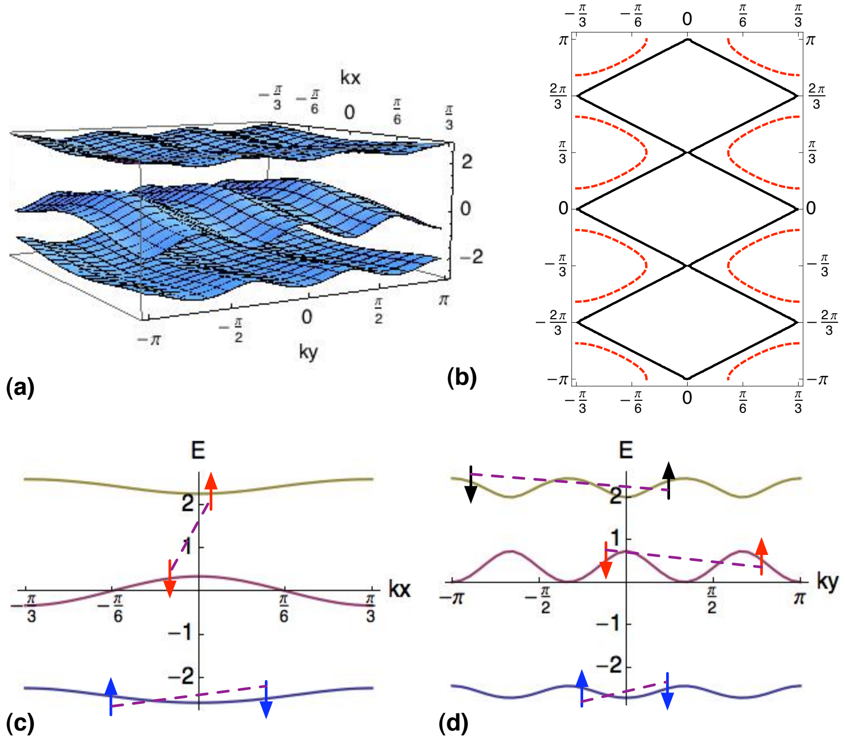

Figure 5.1: (a) Three magnetic bands for $p/q = 1/3$. (b) The Fermi surface of a half-filled (black solid line) and slightly away from half-filled (red dashed line) system. (c) and (d): the band dispersion along the k_x direction with $k_y = 0$ (c) and along the k_y direction with $k_x = 0$ (d). Various possible pairings included in our BCS theory are also illustrated in (c) and (d), which include intra- and inter-band pairing (c), and pairing with nonzero center-of-mass momentum (d).

in the following discussion, to wit

$$\begin{aligned}\psi_{n,k_x,k_y}(x+la,y) &\propto \psi_{n,k_x,k_y+2\pi lp/q}(x,y),\\ \epsilon_{n,k_x,k_y} &= \epsilon_{n,k_x,k_y+2\pi lp/q}.\end{aligned} \tag{5.2}$$

For $p/q = 1/3$, the spectrum and Fermi surface shown in Fig. 5.1(a,b) clearly display a three-fold degeneracy.

In addition to H_0, we consider the on-site interaction between different spin components

$$H_{int} = U \sum_i c^\dagger_{i\uparrow} c^\dagger_{i\downarrow} c_{i\downarrow} c_{i\uparrow}. \tag{5.3}$$

The Hamiltonian for the HH model discussed below is then given by $H_{HH} = H_0 + H_{int}$.

We start by diagonalizing the noninteracting Hamiltonian H_0. First we relabel the sites to reflect the enlargement of the unit cell. For a site $i = (i_x, i_y)$, we let $i_x = j_x q + \beta$, where j_x is an integer labelling the magnetic unit cell and $\beta = 0, \ldots, q-1$ denotes the position of a site within this cell. So, magnetic unit cells are uniquely labelled by j_x and $j_y = i_y$. With this notation we identify $c_{j\beta\sigma} = c_{i\sigma}$. Fourier transformation in the variable j yields $c_{\mathbf{k}\beta\sigma}$, where $\mathbf{k}$ is limited to the MBZ. Diagonalization of H_0 is equivalent to solving Harper's equation [31]. We define a new set of operators $d_{\mathbf{k}n\sigma}$ through $c_{\mathbf{k}\beta\sigma} = \sum_n g^n_\beta(\mathbf{k}) d_{\mathbf{k}n\sigma}$, where $g^n_\beta(\mathbf{k})$ is the βth component of the nth eigenvector of Harper's equation at wavevector $\mathbf{k}$. Upon this definition H_0 becomes

$$H_0 = \sum_{n\mathbf{k}\sigma} \epsilon_{n\mathbf{k}} d^\dagger_{\mathbf{k}n\sigma} d_{\mathbf{k}n\sigma}, \tag{5.4}$$

and one can notice that $d^\dagger_{\mathbf{k}n}$ is the operator that creates a particle in the nth magnetic sub-band at wavevector $\mathbf{k}$. As an example, $\epsilon_{n\mathbf{k}}$ is plotted in Fig. 5.1(a) for $p/q = 1/3$. In terms of $d_{\mathbf{k}n\sigma}$, H_{int} becomes

$$\begin{aligned} H_{int} = U \sum_{\mathbf{k},\mathbf{k}',\mathbf{Q}} \sum_\beta \sum_{n_1,\ldots,n_4} & g^{n_1 *}_\beta\Big(\mathbf{k} + \frac{\mathbf{Q}}{2}\Big) g^{n_2 *}_\beta\Big(-\mathbf{k} + \frac{\mathbf{Q}}{2}\Big) g^{n_3}_\beta\Big(-\mathbf{k}' + \frac{\mathbf{Q}}{2}\Big) g^{n_4}_\beta\Big(\mathbf{k}' + \frac{\mathbf{Q}}{2}\Big) \\ & \times\, d^\dagger_{\mathbf{k}+\frac{\mathbf{Q}}{2},n_1,\uparrow} d^\dagger_{-\mathbf{k}+\frac{\mathbf{Q}}{2},n_2,\downarrow} d_{-\mathbf{k}'+\frac{\mathbf{Q}}{2},n_3,\downarrow} d_{\mathbf{k}'+\frac{\mathbf{Q}}{2},n_4,\uparrow}, \end{aligned} \tag{5.5}$$

where the momentum sum is restricted to the MBZ. We should focus on the "on-shell" Cooper processes. Importantly, due to the q-fold degeneracy, we not only consider $\mathbf{Q} = 0$ terms in Eq. (5.5), but also need to consider all the terms with $\mathbf{Q}_l = (0, 2\pi l p/q)$, where $l = 0, \ldots, q-1$, since $-\mathbf{k}$ and $\mathbf{k} + \mathbf{Q}_l$ also have the same kinetic energy [Eq. (5.2)]. Consequently, nonzero center-of-mass momentum pairing needs to be included as well. Besides, intra-band Cooper pairs have a non-vanishing coupling to the inter-band Cooper pairs. For instance, in Eq. (5.5), if $n_1 = n_2$ but $n_3 \neq n_4$, the interaction coefficient is nonzero.

Hence, intra-band pairing must induce inter-band pairing. All these pairing scenario under consideration are schematically illustrated in Fig. 5.1(c-d), and a comprehensive BCS theory in this problem must treat all these possibilities on an equal footing. Therefore, we introduce totally q^2 order parameters $\vec{\Delta}^l = (\Delta_0^l, \ldots, \Delta_{q-1}^l)$ given by

$$\Delta_\beta^l = -U \sum_{n,n',\mathbf{k}} g_\beta^n\Big(\mathbf{k} + \frac{\mathbf{Q}_l}{2}\Big) g_\beta^{n'}\Big(-\mathbf{k} + \frac{\mathbf{Q}_l}{2}\Big) \langle d_{-\mathbf{k}+\frac{\mathbf{Q}_l}{2},n',\downarrow} d_{\mathbf{k}+\frac{\mathbf{Q}_l}{2},n,\uparrow} \rangle, \tag{5.6}$$

where $l, \beta = 0, \ldots, q-1$ and $\langle \ldots \rangle$ means averaging with respect to the ground state. The site index β denotes q inequivalent sites along the x direction of each magnetic unit cell, and the index l represents the order parameter modulation along the y direction. For instance, for $p/q = 1/3$, there are three different center-of-mass momenta, which are $\mathbf{Q}_{l=0} = (0,0)$, $\mathbf{Q}_{l=1} = (0, 2\pi/3)$ and $\mathbf{Q}_{l=2} = (0, 4\pi/3)$. The real space order parameter for site $i = (i_x, i_y)$ is given by $\Delta_i = \sum_{l=0}^{q-1} \Delta_{i_x(\mathrm{mod} q)}^l \exp(i2\pi l p i_y/q)$, therefore the unit cell in the superfluid phase is enlarged to $q \times q$ in real space (see Fig. 5.2) and the mean-field Hamiltonian is

$$\begin{aligned} H_{MF} &= \sum_{n\mathbf{k}\sigma} \epsilon_{n\mathbf{k}\sigma} d_{n\mathbf{k}\sigma}^\dagger d_{n\mathbf{k}\sigma} \\ &- \sum_{l,\beta} \Big\{ \sum_{n,n',\mathbf{k}} \Big[\Delta_\beta^l g_\beta^{n*}\Big(\mathbf{k} + \frac{\mathbf{Q}_l}{2}\Big) g_\beta^{n'*}\Big(-\mathbf{k} + \frac{\mathbf{Q}_l}{2}\Big) d_{\mathbf{k}+\frac{\mathbf{Q}_l}{2},n,\uparrow}^\dagger d_{-\mathbf{k}+\frac{\mathbf{Q}_l}{2},n',\downarrow}^\dagger + \text{h.c.} \Big] \\ &+ \frac{|\Delta_\beta^l|^2}{U} \Big\}. \end{aligned} \tag{5.7}$$

5.2 Solution to the BCS Model

We start with q^2 random complex numbers as initial Δ_β^l and iteratively solve the BCS mean-field Hamiltonian [Eq. (5.7)] until a self-consistent solution is reached. We find for a convergent solution, the q^2 order parameters are not completely independent. In fact, these q^2 order parameters break up into q sets of q order parameters with the same magnitude. Taking $p/q = 1/3$ or $1/4$ as examples, their relations are summarized in Table 5.1.

Δ^l_β	$\beta = 0$	$\beta = 1$	$\beta = 2$
$l = 0$	a	b	c
$l = 1$	$be^{i\theta_1}$	$ce^{i\theta_1}$	$ae^{i\theta_1}$
$l = 2$	$ce^{i\theta_2}$	$ae^{i\theta_2}$	$be^{i\theta_2}$

Δ^l_β	$\beta = 0$	$\beta = 1$	$\beta = 2$	$\beta = 3$
$l = 0$	a	b	a	b
$l = 1$	c	d	c	d
$l = 2$	$be^{i\theta_1}$	$ae^{i\theta_1}$	$be^{i\theta_1}$	$ae^{i\theta_1}$
$l = 3$	$de^{i\theta_2}$	$ce^{i\theta_2}$	$de^{i\theta_2}$	$ce^{i\theta_2}$

Table 5.1: Pairing order parameters for $p/q = 1/3$ (upper) and $p/q = 1/4$ (lower). a, b, c, and d denotes some complex numbers depending on details, like the fermion density and U/t.

These structures can be understood from the symmetry properties discussed above. The system is invariant under translation by one lattice site along the x direction and a simultaneous translation of k_y by $2\pi p/q$. Under this operation, $\Delta^l_\beta \to \Delta^{l'}_{\beta'}$, where $\beta' = \beta + 1(\text{mod}q)$ and $l' = l + 2(\text{mod}q)$, thus these two order parameters must be equal up to a relative phase. To verify these relations, we show in Fig. 5.4(a) that our numerical solutions satisfy $I_{ll'} = |\vec{\Delta}^{l'}\Gamma\vec{\Delta}^{l\dagger}|/(|\vec{\Delta}^l||\vec{\Delta}^{l'}|) = 1$ for $l' = l + 2(\text{mod}q)$, where Γ is a $q \times q$ matrix with $\Gamma_{ij} = \delta_{i+1(\text{mod}q),j}$. This symmetry imposed relation works for any p/q, which implies that if Δ^0 is nonzero, all $\Delta^{2n(\text{mod}q)}$ are nonzero; i.e. zero and finite-momentum components must coexist.

The self-consistent solution also determines the relative phases. For $p/q = 1/3$, we find six degenerate solutions with $(\theta_1, \theta_2) = (\pm 2\pi/3, \pm 2\pi/3)$,$(0, \pm 2\pi/3)$, $(\pm 2\pi/3, 0)$; for $p/q = 1/4$, we find $\theta_{1,2} = \pm\pi/2$ and either $a, b \neq 0$, $c = d = 0$ or $c, d \neq 0$, $a = b = 0$, therefore there are totally four degenerate solutions. This degeneracy can also be inferred naturally from the geometry of the vortex configuration as displayed in Fig. 5.3. All symmetry-related degenerate configurations are obtainable from each other through translations (corresponding to different choices of the $q \times q$ unit cell) and/or rotations.

The most favorable relative phases can also be understood by a simple

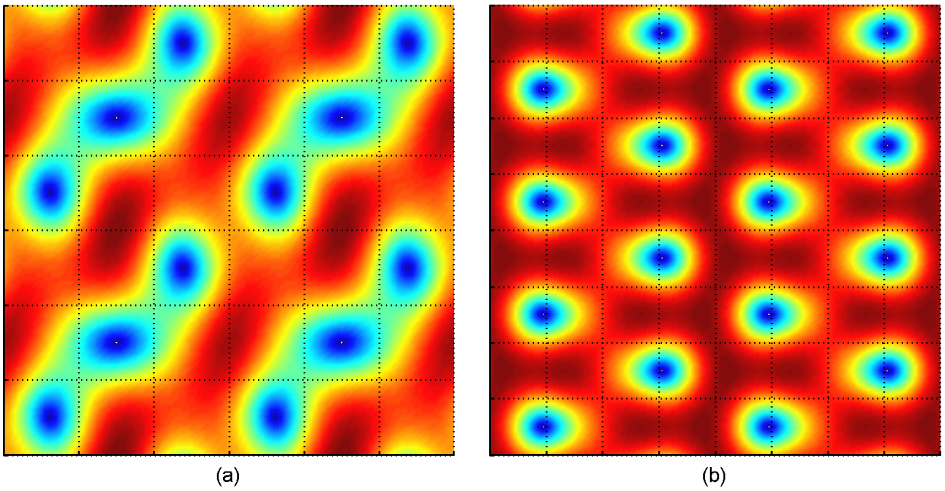

Figure 5.2: Structure of the vortex lattice found from self-consistently solving the BCS mean-field Hamiltonian, where $p/q = 1/3$ for (a) and $p/q = 1/4$ for (b). Blue regions indicate low superfluid density and locate the center of vortex cores. The intersection points of vertical and horizontal dotted lines correspond to lattice sites. In both plots we use $U = -5.5t$ and $n_{\uparrow} = n_{\downarrow} = 1/3$ for (a) and $n_{\uparrow} = n_{\downarrow} = 1/2$ for (b).

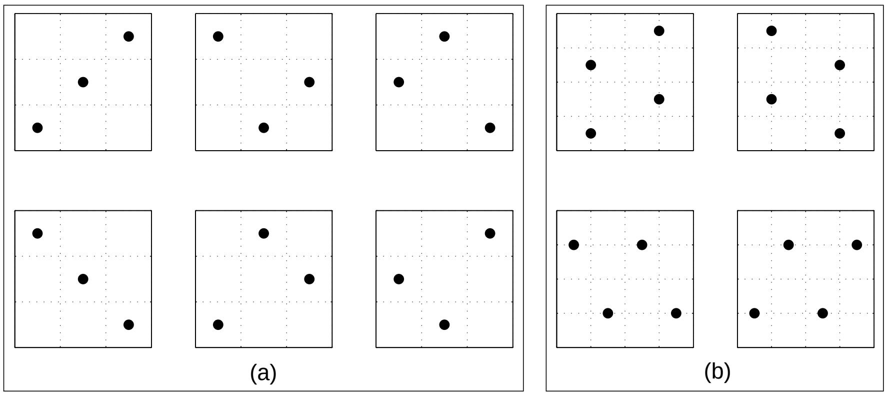

Figure 5.3: Degenerate vortex lattice configurations for $p/q = 1/3$ (a) and $p/q = 1/4$ (b). Filled circles represent the position of vortices. Configurations in the upper row are related to each other by translations (different choices of the $q \times q$ unit cell) and when rotated by 90^o yield those in the lower row.

Ginzburg-Landau (GL) argument. This GL theory should work well particularly nearby the phase transition point discussed below, where the order parameter is small. For those order parameters that definitely coexist, we first write down the most general coupling form between them by momentum conservation, and then determine the most favorable relative phases by minimizing energy. For instance, for $p/q = 1/3$, Δ^0_β, Δ^1_β and Δ^2_β all coexist, and then one can write

$$E_{GL} \propto \sum_\beta \left(\Delta^{0*}_\beta \Delta^{0*}_\beta \Delta^1_\beta \Delta^2_\beta + \Delta^{1*}_\beta \Delta^{1*}_\beta \Delta^0_\beta \Delta^2_\beta + \Delta^{2*}_\beta \Delta^{2*}_\beta \Delta^0_\beta \Delta^1_\beta\right) + \text{c.c.},$$

thus the energy depends on the phases as $\cos(2\theta_1 - \theta_2) + \cos(2\theta_2 - \theta_1) + \cos(\theta_1 + \theta_2)$, and one can easily show that the angles listed above are its minima. For $p/q = 1/4$, Δ^0_β and Δ^2_β definitely coexist, thus one shall write down

$$E_{GL} \propto \sum_\beta \Delta^{0*}_\beta \Delta^{0*}_\beta \Delta^2_\beta \Delta^2_\beta + \text{c.c.},$$

which gives the energy-phase relative as $\cos 2\theta_1$, whose minima occur at $\theta_1 = \pm\pi/2$.

5.2.1 Vortex Configuration

To study the configuration of vortices in the superfluid ground state, we first note that in presence of magnetic field the Wannier wave function at each site can be chosen as [42, 112]

$$w(\mathbf{r} - \mathbf{R_j}) = e^{i2\pi p(x/a)(y/a - j_y)/q} w^0(\mathbf{r} - \mathbf{R_j}), \tag{5.8}$$

where $w^0(\mathbf{r} - \mathbf{R_j})$ is the field-free Wannier wave function. Although this form of the magnetic Wannier function is approximate and valid for small field strengths, it gives the correct Peierls phases for the tight-binding case and will suffice for our purpose of constructing the real space profile of the order parameter $\Delta(\mathbf{r}) = \sum_j \Delta_j w(\mathbf{r} - \mathbf{R_j})$, which is contour-plotted in Fig. 5.2 for two different flux densities. We also verified that the phase of $\Delta(\mathbf{r})$ winds by 2π around each vortex core. There are six (four) space group symmetry-related configurations for Figs. 5.2(a) and 5.2(b), which corresponds to six

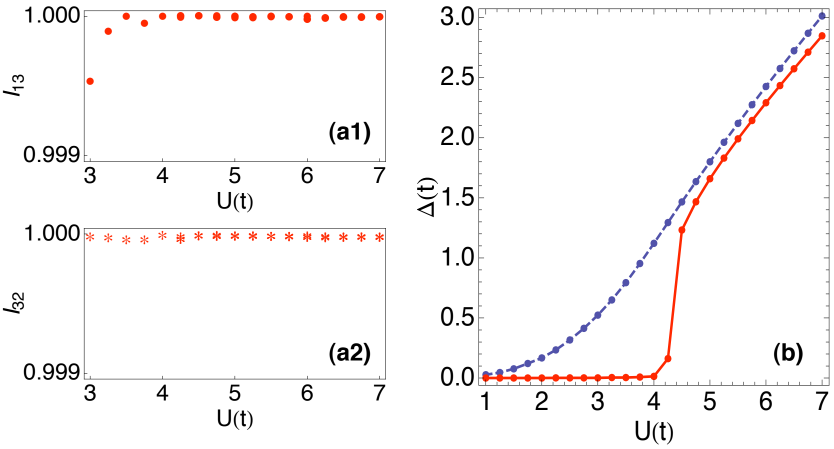

Figure 5.4: (a) For $p/q = 1/3$, I_{02} and I_{21} (see text for definition) are equal to unity within numerical accuracy, which verifies the symmetry relations. (b) Average superfluid order parameter $\Delta = \bar{\Delta}_i$ as a function of U for $p/q = 1/3$, $n = 1/3$ (red solid line) indicates a second-order phase transition and $n = 1/2$ (blue dashed line) does not.

(four) degenerate mean-field solutions (Fig. 5.3). Hence, we have presented a systematical way to determine the configuration of vortices in a BCS superfluid from a microscopic theory, which can be observed with the standard imaging techniques in cold-atom experiments.

5.2.2 Insulator (Semimetal) to Superfluid Transition

For $\phi = p/q$, and for the fermion density of each spin component $n = \nu/q$, where ν is an integer from $1, \ldots, q-1$, the system is usually a Hofstadter insulator in the absence of interactions, except for the case that q is an even integer and $n = 1/2$, where the system is a semimetal since there are Dirac nodes at the Fermi energy. In both cases, since the Fermi energy is either in the band gap (Hofstadter insulator), or the density of states linearly vanishes (Hofstadter semimetal) at the Fermi energy, there is no Cooper instability for infinitesimally small attractive interactions. Thus, it requires a critical interaction strength to turn the system into a paired superfluid through a second-order phase transition, as shown in Fig. 5.4(b). In this calculation, we also fix the fermion density by judging chemical potential. This transition is driven by the competition between pairing-energy gain and the single-particle energy cost to excite particles across the band gap, which was first discussed in Ref. [102] for a lattice system without magnetic field. Without the magnetic field, to realize the transition one needs to tune the interaction close to a Feshbach resonance to achieve strong pairing strength comparable to the band gap; while in this case, since the magnetic band gap is controlled by the original band width t, the transition can be achieved by varying U/t, as routinely done in cold-atom experiments. This transition is accomplished by a change in compressibility and can be measured directly from the *in situ* density profile, which has been successfully used in studying the Bose-Hubbard model.

In conclusion, we studied the structure of a pairing order parameter for spin-1/2 fermions with attractive interactions in a square lattice under a uniform magnetic field. Because the magnetic translation symmetry gives a unique degeneracy in the single-particle spectrum, the pair wave function has both zero and finite momentum components coexisting, and their relative phases are determined by a self-consistent mean-field theory. We presented a microscopic calculation that can determine the vortex lattice structure in the superfluid phase for different flux densities and also discussed the phase transition from a Hofstadter insulator to a superfluid phase.

Chapter 6

Conclusion

The study of ultracold atoms entered a new phase nearly a decade ago when optical lattices loaded with atoms were successfully used to investigate the many-particle physics in these periodic structures and the area has been very active since then. As optical lattices can flexibly be tailored and are defect-free, they provided a perfect setting to test certain quantum mechanical theories related to periodic structures. One important problem in solid state physics is the motion of an electron in a lattice under a magnetic field. With optical lattices now it is possible to study this old problem in the cold-atom context. Since the atoms used in cold-atom experiments are neutral, rotation or other methods involving atom-light interactions should be introduced in order to simulate the effects of magnetic field on a charged particle. The physics in the limit of high magnetic field is very rich including the appearance of the fractal single-particle energy spectrum and analogues of fractional quantum Hall states. Researchers are striving to reach this high-field regime by continuously developing new schemes.

Our work presented in this thesis can be considered a modest contribution to this attractive branch of physics. A common theme that appears in almost all of the phenomena we investigated is the single-particle Hofstadter spectrum. Although the model leading to this spectrum is simple, it gives rise to many interesting and diverse phenomena both for noninteracting and interacting particles. In the context of noninteracting particles, we proposed a scheme for the observation of the Hofstadter butterfly which depends on a measurement of the density profile of trapped fermions. The gap regions in the spectrum will appear as plateaus in the density profile. With this technique it is also possible to measure the quantum Hall conductance of these gaps without doing transport experiments. We also studied the effects of a synthetic magnetic field on interacting systems. We investigated the superfluid-Mott insulator transition under rotation using mean-field approximation and found an analytical formula for the phase boundary which reflects the complex structure of the single-particle spectrum. We also predicted that a novel phase of coexisting Mott insulator and bosonic Laughlin states should appear near the transition boundary since such a state will be energetically favorable compared to the superfluid state for high enough interaction strengths. We supported our prediction with an exact diagonalization of a small system and variational Monte Carlo calculations for larger systems. As for interacting fermions, we considered a BCS-type pairing of them in a lattice under a large magnetic field. In this study, it turned out that single-particle degeneracies play an important role in determining the nature of pairing and the vortex lattice structure for the paired fermionic superfluid phase emerges naturally from a microscopic theory. We hope that rapidly developing experimental techniques for attaining high effective magnetic fields will allow us to test our predictions soon.

Bibliography

[1] K. B. Davis, M.-O. Mewes, M. R. Andrews, N. J. van Druten, D. S. Durfee, D. M. Kurn, and W. Ketterle, Phys. Rev. Lett. **75**, 3969 (1995).

[2] M. H. Anderson, J. R. Ensher, M. R. Matthews, C. E. Wieman, and E. A. Cornell, Science **269**, 198 (1995).

[3] A. Einstein, Sitzungsberichte der Preussischen Akademie der Wissenschaften, Physikalisch-mathematische Klasse (1924), p. 261; (1925), p. 3.

[4] M. Greiner, O. Mandel, T. Esslinger, T. W. Hänsch, and I. Bloch, Nature **415**, 39 (2002).

[5] M. P. A. Fisher, P. B. Weichman, G. Grinstein, and D. S. Fisher, Phys. Rev. B **40**, 546 (1989).

[6] D. Jaksch, C. Bruder, J. I. Cirac, C. W. Gardiner, and P. Zoller, Phys. Rev. Lett. **81**, 3108 (1998).

[7] M. Lewenstein, A. Sanpera, V. Ahufinger, B. Damski, A. Sen, and U. Sen, Adv. Phys. **56**, 243 (2007).

[8] I. Bloch, J. Dalibard, and W. Zwerger, Rev. Mod. Phys. **80**, 885 (2008).

[9] C. J. Pethick and H. Smith, *Bose-Einstein Condensation in Dilute Gases*, 2nd ed. (University Press, Cambridge, 2008).

[10] D. S. Rokhsar and B. G. Kotliar, Phys. Rev. B **44**, 10328 (1991).

[11] K. Sheshadri, H. R. Krishnamurthy, R. Pandit, and T. V. Ramakrishnan, Europhys. Lett. **22**, 257 (1993).

[12] D. van Oosten, P. van der Straten, and H. T. C. Stoof, Phys. Rev. A **63**, 053601 (2001).

[13] N. R. Cooper, Adv. Phys. **57**, 539 (2008).

[14] A. L. Fetter, Rev. Mod. Phys. **81**, 647 (2009).

[15] E. Lieb and R. Seiringer, Commun. Math. Phys. **264**, 505 (2006).

[16] N. R. Cooper, S. Komineas, and N. Read, Phys. Rev. A **70**, 033604 (2004).

[17] W. H. Kleiner, L. M. Roth, and S. H. Autler, Phys. Rev. **133**, A1226 (1964).

[18] N. R. Cooper, N. K. Wilkin, and J. M. F. Gunn, Phys. Rev. Lett. **87**, 120405 (2001).

[19] N. R. Cooper and N. K. Wilkin, Phys. Rev. B **60**, R16279 (1999).

[20] N. Regnault and Th. Jolicoeur, Phys. Rev. B **69**, 235309 (2004).

[21] C.-C. Chang, N. Regnault, Th. Jolicoeur, and J. K. Jain, Phys. Rev. A **72**, 013611 (2005).

[22] K. W. Madison, F. Chevy, W. Wohlleben, and J. Dalibard, Phys. Rev. Lett. **84**, 806 (2000).

[23] P. C. Haljan, I. Coddington, P. Engels, and E. A. Cornell, Phys. Rev. Lett. **87**, 210403 (2001).

[24] P. Engels, I. Coddington, P. C. Haljan, and E. A. Cornell, Phys. Rev. Lett. **89**, 100403 (2002).

[25] V. Schweikhard, I. Coddington, P. Engels, V. P. Mogendorff, and E. A. Cornell, Phys. Rev. Lett. **92**, 040404 (2004).

[26] V. Bretin, S. Stock, Y. Seurin, and J. Dalibard, 2004, Phys. Rev. Lett. **92**, 050403 (2004).

[27] S. Tung, V. Schweikhard, and E. A. Cornell, Phys. Rev. Lett. **97**, 240402 (2006).

[28] J. W. Reijnders and R. A. Duine, Phys. Rev. A **71**, 063607 (2005).

[29] M. Hafezi, A. S. Sørensen, E. Demler, and M. D. Lukin, Phys. Rev. A **76**, 023613 (2007).

[30] R. A. Williams, S. Al-Assam, and C. J. Foot, Phys. Rev. Lett. **104**, 050404 (2010).

[31] D. R. Hofstadter, Phys. Rev. B **14**, 2239 (1976).

[32] D. Jaksch and P. Zoller, New J Phys. **5**, 56 (2003).

[33] E. J. Mueller, Phys. Rev. A **70**, 041603 (2004).

[34] K. Osterloh, M. Baig, L. Santos, P. Zoller, and M. Lewenstein, Phys. Rev. Lett. **95**, 010403 (2005).

[35] J. Ruseckas, G. Juzeliūnas, P. Öhberg, and M. Fleischhauer, Phys. Rev. Lett. **95**, 010404 (2005).

[36] G. Juzeliūnas, P. Öhberg, J. Ruseckas, and A. Klein, Phys. Rev. A **71**, 053614 (2005).

[37] Q. Zhang, J. Gong, and C. H. Oh, Pys. Rev. A **79**, 043632 (2009).

[38] K. J. Günter, M. Cheneau, T. Yefsah, S. P. Rath, and J. Dalibard, Phys. Rev. A **79**, 011604(R) (2009).

[39] I. B. Spielman, Phys. Rev. A **79**, 063613 (2009).

[40] Y.-J. Lin, R. L. Compton, K. Jimenez-Garcia, J. V. Porto, and I. B. Spielman, Nature, **462**, 628 (2009).

[41] R. Peierls, Z. Physik **80**, 763 (1933).

[42] J. M. Luttinger, Phys. Rev. **84**, 814 (1951).

[43] P. G. Harper, Proc. Phys. Soc. (London) A **68**, 874 (1955).

[44] E. Brown, Phys. Rev. **133**, A1038 (1964).

[45] J. Zak, Phys. Rev. **134**, A1602 (1964); **134**, A1607 (1964); **136**, A1647 (1964).

[46] D. Langbein, Phys. Rev. **180**, 633 (1969).

[47] H. J. Schneider-Muntau, J. Toth, and H. W. Weijers, IEEE Trans. Appl. Supercond. **14**, 1245 (2004).

[48] C. Albrecht, J. H. Smet, K. von Klitzing, D. Weiss, V. Umansky, and H. Schweizer, Phys. Rev. Lett. **86**, 147 (2001).

[49] J. Callaway, *Quantum Theory of the Solid State*, 2nd ed. (Academic, New York, 1991).

[50] D. Xiao, M. C. Chang, and Q. Niu, Rev. Mod. Phys. **82**, 1959 (2010).

[51] I. Dana, Y. Avron, and J. Zak, J. Phys. C **18**, L679 (1985).

[52] G. M. Obermair and H.-J. Schellnhuber, Phys. Rev. B **23**, 5185 (1981).

[53] H.-J. Schellnhuber, G. M. Obermair, and A. Rauh, Phys. Rev. B **23**, 5191 (1981).

[54] D. J. Thouless, Phys. Rev. B **28**, 4272 (1983).

[55] R. O. Umucalılar and M. Ö. Oktel, Phys. Rev. A **76**, 055601 (2007).

[56] M. Köhl, H. Moritz, T. Stöferle, K. Günter, and T. Esslinger, Phys. Rev. Lett. **94**, 080403 (2005).

[57] T. Müller, S. Fölling, A. Widera, and I. Bloch, Phys. Rev. Lett. 99, 200405 (2007).

[58] W. V. Liu and C. Wu, Phys. Rev. A **74**, 013607 (2006).

[59] C. Wu, D. Bergman, L. Balents, and S. Das Sarma, Phys. Rev. Lett. 99, 070401 (2007).

[60] K. Wu and H. Zhai, Phys. Rev. B **77**, 174431 (2008).

[61] L. Wang, X. Dai, S. Chen, and X. C. Xie, Phys. Rev. A **78**, 023603 (2008).

[62] C. Wu and S. Das Sarma, Phys. Rev. B **77**, 235107 (2008).

[63] V. M. Stojanovic, C. Wu , W. V. Liu, and S. Das Sarma, Phys. Rev. Lett. **101**, 125301 (2008).

[64] C. Wu, Phys. Rev. Lett. **101**, 186807 (2008).

[65] A. Isacsson and S. M. Girvin, Phys. Rev. A **72**, 053604 (2005).

[66] C. Wu, W. V. Liu, J. Moore, and S. Das Sarma, Phys. Rev. Lett. **97**, 190406 (2006).

[67] E. Zhao and W. V. Liu, Phys. Rev. Lett. **100**, 160403 (2008).

[68] C. Wu, Phys. Rev. Lett. **100**, 200406 (2008).

[69] R. O. Umucalılar and M. Ö. Oktel, Phys. Rev. A **78**, 033602 (2008).

[70] R. O. Umucalılar and E. J. Mueller, Phys. Rev. A **81**, 053628 (2010).

[71] M. Niemeyer, J. K. Freericks, and H. Monien, Phys. Rev. B **60**, 2357 (1999).

[72] M. Ö. Oktel, M. Niţă, and B. Tanatar, Phys. Rev. B **75**, 045133 (2007).

[73] W. Krauth, N. Trivedi, and D. Ceperley, Phys. Rev. Lett. **67**, 2307 (1991).

[74] A. S. Sørensen, E. Demler, and M. D. Lukin, Phys. Rev. Lett. **94**, 086803 (2005).

[75] R. Bhat, L. D. Carr, and M. J. Holland, Phys. Rev. Lett. **96**, 060405 (2006).

[76] R. N. Palmer and D. Jaksch, Phys. Rev. Lett. **96**, 180407 (2006).

[77] R. N. Palmer, A. Klein, and D. Jaksch, Phys. Rev. A **78**, 013609 (2008).

[78] R. Bhat, B. M. Peden, B. T. Seaman, M. Krämer, L. D. Carr, and M. J. Holland, Phys. Rev. A **74**, 063606 (2006).

[79] R. Bhat, M. Krämer, J. Cooper, and M. J. Holland, Phys. Rev. A **76** 043601 (2007).

[80] G. Möller and N. R. Cooper, Phys. Rev. Lett. **103**, 105303 (2009).

[81] D. J. Thouless, M. Kohmoto, M. P. Nightingale, and M. den Nijs, Phys, Rev. Lett. **49**, 405 (1982).

[82] A. H. MacDonald, Phys. Rev. B **29**, 6563 (1984).

[83] H. Aoki, Phys. Rev. Lett. **55**, 1136 (1985).

[84] W. Chen, M. P. A. Fisher, and Y.-S. Wu, Phys. Rev. B **48**, 13749 (1993).

[85] X.-G. Wen and Y.-S. Wu, Phys. Rev. Lett. **70**, 1501 (1993).

[86] F. F. Assaad and S. Biskamp, Phys. Rev. B **51**, 1605 (1995).

[87] D. Pfannkuche and A. H. MacDonald, Phys. Rev. B **56**, R7100 (1997).

[88] J. Ye and S. Sachdev, Phys. Rev. Lett. **80**, 5409 (1998).

[89] R. B. Laughlin, Phys. Rev. Lett. **50**, 1395 (1983).

[90] F. D. M. Haldane and E. H. Rezayi, Phys. Rev. B **31** 2529 (1985).

[91] E. J. Mueller, T.-L. Ho, M. Ueda, and G. Baym, Phys. Rev. A **74**, 033612 (2006).

[92] F. D. M. Haldane, Phys. Rev. Lett. **55**, 2095 (1985).

[93] H. Yokoyama and H. Shiba, J. Phys. Soc. Jpn **56**, 1490 (1987).

[94] N. Trivedi and D. M. Ceperley, Phys. Rev. B **41**, 4552 (1990).

[95] S. Fahy, X. W. Wang, and S. G. Louie, Phys. Rev. B **42**, 3503 (1990).

[96] *Quantum Monte Carlo Methods in Physics and Chemistry*, edited by M. P. Nightingale and C. J. Umrigar, NATO Science Series, Series C: Mathematical and Physical Sciences, Vol. 525 (Kluwer Academic, Boston, 1999).

[97] V. Ambegaokar and M. Troyer, Am. J. Phys. **78**, 150 (2010).

[98] R. O. Umucalılar, H. Zhai, and M. Ö. Oktel, Phys. Rev. Lett. 100, 070402 (2008).

[99] J. Kellendonk, Commun. Math. Phys. **258**, 751 (2005).

[100] P. Středa, T. Jonckheere, and T. Martin, Phys. Rev. Lett. **100**, 146804 (2008).

[101] L. Pitaevskii and S. Stringari, *Bose-Einstein Condensation* (Clarendon Press, Oxford, 2003), Ch. 16.2.

[102] H. Zhai and T. L. Ho, Phys. Rev. Lett. **99**, 100402 (2007).

[103] T. L. Ho and Q. Zhou, Phys. Rev. Lett. **99**, 120404 (2007).

[104] T. L. Ho and C.V. Ciobanu, Phys. Rev. Lett. **85**, 4648 (2000).

[105] P. Středa, J. Phys. C **15** L717 (1982).

[106] C. J. Wu, H. D. Chen, J. P. Hu, and S. C. Zhang, Phys. Rev. A **69**, 043609 (2004).

[107] D. S. Goldbaum and E. J. Mueller, Phy. Rev. A **77** 033629 (2008); **79** 021602 (2009).

[108] K. Kasamatsu, Phys. Rev. A **79**, 021604(R) (2009).

[109] T. Durić and D. K. K. Lee, Phys. Rev. B **81**, 014520 (2010).

[110] M. M. Maśka, Phys. Rev. B **66**, 054533 (2002).

[111] H. Zhai, R. O. Umucalılar, and M. Ö. Oktel, Phys. Rev. Lett. **104**, 145301 (2010).

[112] I. Dana and J. Zak, Phys. Rev. B **28**, 811 (1983).